Erdely, P.; Staron, P.; Stark, A.; Klein, T.; Clemens, H.; Mayer, S.:
In situ and atomic-scale investigations of the early stages of γ precipitate growth in a supersaturated intermetallic Ti-44Al-7Mo (at.%) solid solution.
In: Acta Materialia. Vol. 164 (2019) 110 - 121.
First published online by Elsevier: 24.10.2018

https://dx.doi.org/10.1016/j.actamat.2018.10.042

In situ and atomic-scale investigations of the early stages of γ precipitate growth in a supersaturated intermetallic Ti-44Al-7Mo (at.%) solid solution

Petra Erdely [a,*], Peter Staron [b], Andreas Stark [b], Thomas Klein [a,1], Helmut Clemens [a], Svea Mayer [a]

[a] Department of Physical Metallurgy and Materials Testing, Montanuniversität Leoben, Roseggerstr. 12, A-8700 Leoben, Austria; helmut.clemens@unileoben.ac.at; svea.mayer@unileoben.ac.at.

[b] Institute of Materials Research, Helmholtz-Zentrum Geesthacht, Max-Planck-Str. 1, D-21502 Geesthacht, Germany; peter.staron@hzg.de; andreas.stark@hzg.de.

* Corresponding author. Tel.: +43 3842 402 4204; fax: +43 3842 402 4202; petra.erdely@unileoben.ac.at.

[1] Present address: Materials Center Leoben Forschung GmbH, Roseggerstr. 12, A-8700 Leoben, Austria; thomas.klein@mcl.at.

Abstract

Intermetallic β-stabilised γ-TiAl based alloys offer novel opportunities for microstructural design. This paper investigates the growth behaviour of γ precipitates from a supersaturated β_o matrix in a β-homogenised Ti-44Al-7Mo (at.%) alloy. Combining *in situ* high-energy X-ray diffraction and small-angle scattering at a synchrotron radiation source with atom probe tomography as a direct imaging technique, the early stages of γ precipitate growth are characterised for the first time. The results show that the $\beta_o \rightarrow \gamma$ phase transformation occurs without the formation of an intermediate phase. At a heating rate of 10 $K \cdot min^{-1}$, first diffusional processes that can be ascribed to the $\beta_o \rightarrow \gamma$ phase transformation commence at about 450 °C. Elemental redistribution controls the growth of the γ precipitates, which is connected with the introduction of misfit-induced strain fields around the initially coherent γ particles. Further heating results in the loss of coherency between the disc-shaped γ precipitates and the β_o matrix. The presented findings advance the fundamental understanding of the $\beta_o \rightarrow \gamma$ phase transformation in γ-TiAl based alloys and provide

quantitative data for the design of refined microstructures in the course of technological heat treatments.

Keywords

Titanium aluminides; High-energy X-ray diffraction; Small-angle X-ray scattering; Atom probe tomography (APT); Phase transformation

1. Introduction

Intermetallic γ-TiAl based alloys satisfy many of the key requirements for structural lightweight high-temperature applications in aerospace and automotive industries. At a low density of roughly 4 $g \cdot cm^{-3}$, they exhibit a high specific Young's modulus and yield strength at elevated temperatures combined with good creep properties and oxidation resistance [1]. The class of β-stabilised γ-TiAl based alloys additionally offers improved processing characteristics in terms of hot workability due to the presence of the disordered body-centred cubic β phase (A2 structure) at high temperatures [2–6]. Recent research has furthermore highlighted novel opportunities for microstructural design based on the β/β_o phase [3,7–10]. As molybdenum is associated with a particularly strong β-stabilising effect [11–13], ternary Ti-Al-Mo alloys represent excellent model alloy systems to assess the prospects of a wide range of microstructures and explore potential solutions to the major limitations of γ-TiAl based alloys: their low tensile ductility and fracture toughness at ambient temperature [1,7,9].

Over the last decades, a growing body of literature has centred on phase equilibria and phase transformations in various Ti-Al-Mo alloys [12,14–22]. Recently, the ternary Ti-44Al-7Mo (at.%) alloy has attracted interest, as research has shown that certain heat treatments on cast material entail a substantial refinement of the microstructure [8,10,23] as well as a significant increase in hardness [8,10]. Ti-44Al-7Mo (at.%) specimens that are homogenised in the β single-phase region and subsequently water-quenched (WQ)

specifically provide a promising starting condition for ensuing continuous heating [10] or annealing treatments below the eutectoid temperature [8,10,23]. These heat treatments provoke the formation of homogeneously distributed precipitates on the submicrometre-scale [8,10,23]. Transmission electron microscopy (TEM) investigations have verified the $L1_0$ structure of these γ particles and described their orientation relationship with the parent β_o phase (B2 structure) as $<111>\beta_o \{110\}\beta_o \parallel <101>\gamma \{111\}\gamma$ [10]. Studies based on 3D characterisation techniques have furthermore revealed that in long-term annealed conditions, γ and β_o form fully interconnected networks with phase fractions of 55 and 45 vol.%, respectively [23]. In sum, a number of preliminary studies have focused on either the β-homogenised initial or annealed final conditions, highlighting technologically promising features. However, the early stages and underlying mechanisms of the $\beta_o \rightarrow \gamma$ transformation have never been studied in detail in high-Mo containing γ-TiAl based alloys.

To date, only few researchers have explicitly addressed the formation of γ from a β or β_o matrix stabilised by Mo. Singh et al. [15] discussed the $\beta \rightarrow \beta + \gamma$ reaction in the framework of an analysis of the solidification structures of various Ti-(44-50)Al-(2-6)Mo (at.%) alloys. In their Mo-rich alloy variants, they observed lenticular γ structures upon the transition from the $(\alpha + \beta)$ to the $(\alpha + \beta + \gamma)$ region. The direct precipitation of γ in β in the course of a single-step heat treatment was described by the same authors elsewhere [24]. More recently, finely precipitated γ has been reported to occur in β/β_o upon annealing of the so-called TNM alloy of a nominal chemical composition of Ti-43.5Al-4Nb-1Mo-0.1B (at.%) and its derivatives [25–27]. Further previous work, though, has been largely limited to other materials systems, i.e. notably Nb-bearing alloys. For example, in their seminal work on Ti-44Al-8Nb (at.%) and Ti-44Al-4Nb-4Zr-0.2Si (at.%) alloys, Cheng and Loretto [6] set out two potential mechanisms of γ formation during cooling from the $(\alpha + \beta)$ region. They proposed that the metastable β phase transforms partially to γ either by a process similar to the discontinuous coarsening of γ lamellae or a direct nucleation of the γ grains. Goyel et al. [28]

found that in Ti-45Al-18Nb (at.%) alloys cooling from the β-single phase field entails two discrete stages of γ nucleation, which take place at different nucleation sites.

For the past decades, research has tended to focus on the formation of γ from the disordered β matrix [29]. Only recently, Song et al. [29,30] and Klein et al. [26] have studied the phase transformations during reheating of a quenched Ti-45Al-8.5Nb-0.2W-0.2B-0.02Y (at.%) and a Ti-43.32Al-4.02Nb-0.96Mo-0.12B-0.34C-0.31Si (at.%) alloy and suggested a direct nucleation of nanometre-scale γ from supersaturated β_o in their *ex situ* studies of selected heat-treated conditions. However, as the high Nb content of these alloys involves the appearance of further phases and microstructural constituents such as α_2 ($D0_{19}$ structure), α_2' martensite, massive γ, and ω_o ($B8_2$ structure), the knowledge gained from these latter studies cannot be directly applied to Ti-Al-Mo alloys. Furthermore, γ growth sequences have never been studied by means of *in situ* methods, although exactly this knowledge is vital to the comprehension of early growth stages as well as the optimisation of technological heat treatments.

This paper seeks to elucidate the growth behaviour of γ precipitates in a β-homogenised Ti-44Al-7Mo (at.%) alloy. Heating experiments were conducted in a dilatometer setup at a sychrotron radiation source. While *in situ* HEXRD was used to study the structural changes in the prevalent phases, *in situ* small-angle X-ray scattering (SAXS) and atom probe tomography (APT) were combined to characterise the early stages of growth in terms of size, shape and chemical composition of the nanometre-scale precipitates.

2. Material and methods

2.1 Alloy composition and processing

The alloy of a nominal chemical composition of Ti-44Al-7Mo (at.%) was prepared by GfE Metalle and Materialien GmbH, Germany, by means of ingot metallurgy [9]. Cast ingots were

hot-isostatically pressed (HIP) at 1200 °C and 200 MPa for 240 min to close any residual casting porosity. In this cast/HIP condition, the actual chemical composition of the ingot used in this study was determined by means of X-ray fluorescence spectroscopy. It amounted to Ti-43.39Al-6.92Mo-0.02B (at.%). From the cast/HIP ingot, cylindrical specimens of 5 mm in diameter and 13 mm in length were machined by means of spark erosion. Using a high temperature chamber furnace Carbolite RHF 1600, these specimens were homogenised in the β single-phase region at 1450 °C for 30 min followed by WQ [8]. Prior to the ensuing experiments, an outer layer of 500 µm was removed from the specimens, leading to an effective reduction of the diameter to 4 mm.

2.2 *In situ* diffraction and scattering experiments

2.2.1 General experimental setup

The HEXRD and SAXS experiments were conducted at the P07 high-energy materials science (HEMS) beamline operated by the Helmholtz-Zentrum Geesthacht (HZG) at PETRA III at the Deutsches Elektronen Synchrotron (DESY), Germany. Using a modified quenching and deformation dilatometer DIL805A/D by TA Instruments, Germany, β-homogenised specimens were heated under Ar atmosphere at a constant rate of 10 $K \cdot min^{-1}$. The temperature was measured by means of type S thermocouples spot-welded onto the specimens. Regarding the incident X-ray beam, a mean photon energy of 100 keV ($\lambda = 0.124$ Å) was selected. For both the HEXRD and SAXS experiments, a Perkin Elmer (PE) XRD 1621 flat panel detector with a pixel matrix of 2048 × 2048 and a pixel size of 200 × 200 μm^2 was used. The specimens were probed in transmission geometry.

2.2.2 Specifics of the HEXRD experiments

The PE detector was positioned centrically at a distance of 1597 mm from the specimens. The cross-section of the incident X-ray beam was 0.5 × 0.5 mm^2. This setup, which was calibrated with LaB_6 powder, allowed capturing complete diffraction patterns up to a Bragg

angle 2θ of roughly 7°. The 2D diffraction patterns recorded during an exposure time of 3 s were azimuthally integrated with the aid of the software package Fit2D [31]. Individual peaks were fitted with Pseudo-Voigt functions using the software package MATLAB [32].

2.2.3 Specifics of the SAXS experiments

The PE detector was placed at a distance of 10852 mm from the specimens, and a beam stop with a diameter of 1 mm was used. The cross-section of the incident beam was set to 0.32×0.32 mm^2. This setup was calibrated using a silver behenate standard. SAXS patterns were recorded continuously during the heating experiments with an exposure time of 10 s. For the further data evaluation, the 2D patterns were corrected for background scattering, electronic noise, and transmission. As the anisotropy observed in the SAXS signal was small, the detector images were azimuthally integrated with the aid of the software package Fit2D [31]. Based on the results of the APT measurements (see sections 2.3 and 3.3.1), which gave the chemical compositions of the phases as well as an approximate precipitate volume fraction f at 680 °C, the absolute macroscopic scattering cross-sections were calibrated. The scattering contrast $\Delta\eta$, which represents the difference in the scattering length densities of the matrix and the particles, was also calculated based on the APT data. For a first approximation, $\Delta\eta$ was set to the constant value of 1.69×10^{10} cm^{-1}. The scattering curves were fitted using the programme SANSFit, which is based on a least-squares procedure as described in Ref. [33]. The particles were first modelled as spheres to obtain an equivalent radius R_{eq}. This radius was used to trace the precipitate growth kinetics without the necessity of introducing further assumptions on the potentially changing particle shape. The scattering curve recorded at 680 °C was also fitted by modelling the particles as prolate ellipsoids of revolution with axes of $2R_0$ and $2\mu R_0$. The aspect ratio μ was set to 0.37 as suggested by the APT results. A constant background was added to the macroscopic scattering cross-section as a free parameter.

The integration of the macroscopic differential scattering cross-section $\mathrm{d}\Sigma/\mathrm{d}\Omega$ according to

$$Q = 4\pi \int_{q_{\min}=0}^{q_{\max}=\infty} \frac{d\Sigma}{d\Omega}(q) q^2 dq \qquad \text{(Eq. 1)}$$

yields the integrated intensity Q. The length of the scattering vector in Eq. 1 is given by $|\boldsymbol{q}| = q = (4\pi/\lambda)\cdot\sin\theta$, 2θ representing the Bragg angle of the scattered photons. Q is proportional to the product of the scattering contrast $\Delta\eta$ and the volume fraction f of the scattering centres. In this paper, the observed intensities were integrated over a limited q-range of 0.1 to 2 nm^{-1}. Therefore, the resulting integrated intensity, which was termed Q', gives limited information about the scattering particles that can only be used for comparisons in a more qualitative way.

2.3 Atom probe tomography

APT was conducted using a local electron atom probe (LEAP™) 3000X HR from Cameca Instruments Inc. with a detector efficiency of roughly 0.37. The experiments were carried out using laser pulsing mode at a temperature of 60 K, a pulse repetition rate of 250 kHz, and a pulse energy of 0.4 nJ. The generated data were analysed using the Cameca IVAS™ 3.6.8 software package. Peak overlaps were considered by means of peak deconvolution based on the knowledge of the natural abundance of the detected ions. The needle-shaped APT specimens were prepared according to a three step procedure as described in Ref. [34]. This procedure involved the electrolytic etching of precision cut blanks using 5% perchloric acid in acetic acid. After generating a rough tip shape, 2% perchloric acid in butoxyethanol was used for etching and the final shaping of the tip.

2.4 Microstructural characterisation

The microstructure was characterised by means of scanning electron microscopy (SEM) using a Zeiss EVO50 and a FEI Versa 3D DualBeam™. All images were taken in the back-scattered electron (BSE) mode, in which the β_o phase shows the brightest, the γ phase the

darkest, and the α_2 phase an intermediate contrast. The metallographic specimens were prepared as described by Schloffer et al. [35].

3. Results

3.1 Microstructure

Figure 1 illustrates the microstructural evolution of the cast/HIP Ti-44Al-7Mo (at.%) alloy in the course of the β homogenisation and subsequent heating/annealing treatment. In the cast/HIP condition (Fig. 1a), large β_o grains are intersected by lath-like γ grains as well as a small number of α_2 grains. The homogenisation treatment in the β single-phase region at 1450 °C for 30 min provokes the dissolution of γ and α_2, the latter of which first disorders to α (A3 structure) upon heating. Ensuing WQ on the one hand suppresses the re-precipitation of γ and α/α_2, and on the other hand appears to preclude a massive or martensitic transformation [10]. As a result, the single-phase β_o microstructure is retained at room temperature. In this β-homogenised condition (Fig. 1b), large β_o grains are discernible in the SEM-BSE images based on their orientation contrast. Grain boundaries appear straight and typically meet at an angle of 120°. At this point it should be noted, though, that the statements made above hold true only for the bulk of the specimens. Due to technological reasons, surface-near areas experienced slightly different cooling conditions. Immediately before entering the water bath during the WQ process, air cooling decreased the temperature in the outer zone to values below the β-transus temperature, which marks the entering of the (α + β) region. Consequently, unlike the inner zone of the specimens, this outer zone was not quenched from the β single-phase region. The result is an outer layer of several 100 µm in thickness, which is characterised by α_2 laths within the β_o matrix (Fig. 1b, insert). Prior to the ensuing heating/annealing experiments, this layer was removed by grinding.

Figure 1c shows the microstructure of a β-homogenised specimen that was heated to 900 °C at a constant rate of 10 $K \cdot min^{-1}$ and then rapidly cooled. Fine γ particles with dimensions on the submicrometre-scale and a high number density have precipitated. They appear homogeneously distributed within the β_o matrix. Larger γ precipitates cover the β_o grain boundaries as a result of the accelerated nucleation. Figure 1d shows the microstructure of a β-homogenised specimen that was isothermally annealed at 900 °C for 100 h followed by WQ. Compared to Fig. 1c, the γ precipitates have coarsened. Considering the dimensions and the annealing time, however, they are still fairly small and give rise to a homogeneous microstructure. Comparing the overview image in Fig. 1d to the insert in Fig. 1a, which corresponds to the same level of magnification, the microstructural refinement through the β homogenisation and subsequent annealing treatment becomes apparent. While at first sight this refinement seems to extend only to the γ phase, it should be noted that in long-term annealed conditions γ and β_o have been found to form fully interconnected networks [23].

The peculiar arrangement of the axes of the γ precipitates (Figs. 1c and d, inserts) indicates the presence of a well-defined orientation relationship between γ and β_o. TEM investigations on β-homogenised Ti-44Al-7Mo (at.%) specimens heated to 830 °C and annealed at 1000 °C for 164 h have allowed describing this orientation relationship with the parent β_o phase as $<111>\beta_o$ $\{110\}\beta_o \parallel <101>\gamma$ $\{111\}\gamma$ [10]. The parallel alignment of the γ and β_o planes and directions with the highest atomic densities has also been reported for other γ-TiAl based alloys following the precipitation of γ from β/β_o [14,30,36,37].

3.2 *In situ* observation of the structural evolution during heating

The coarse-grained nature of the β-homogenised condition (Fig. 1b), in combination with a rather small X-ray beam size, gives rise to a spotted diffraction pattern (Fig. 2a). Grains that fulfil the Ewald condition yield strong reflections on the corresponding Debye-Scherrer rings.

Simultaneously, some β_o grains may not perfectly match, but still lie close to the Ewald condition. As argued by Liss et al. [38], these selected grains are likely to cause thermal diffuse scattering as observed in Fig. 2a, reflecting the symmetry of the crystal structure.

To facilitate the comprehension of the $\beta_o \rightarrow \gamma$ phase transformation path, the 2D diffraction patterns recorded during the *in situ* heating experiment were azimuthally integrated. The resulting diffractograms were then plotted in such a way as to trace the evolution of intensity as a function of the Bragg angle 2θ and temperature (Fig. 2b). As could be expected from the 2D diffraction pattern, the initial condition is characterised by strong β_o reflections, whose relative intensities differ from the arrangement in a powder pattern due to the relatively small number of probed grains. The presence of the β_o-100 superstructure reflection, which is shown in the insert in Fig. 2b, proves that WQ did not completely suppress the $\beta \rightarrow \beta_o$ ordering transformation.

Besides the β_o reflections, weak α_2 reflections can be observed in both Figs. 2a and b. These reflections may stem from α_2 laths in some residual parts of the outer zone of the specimens (Fig. 1b) or α_2 laths along grain boundaries and cracks as reported in Ref. [17]. While they are present during the entire heating experiment, they are not visibly altered. Since the volume fraction of the α_2 grains is very small, they cannot be expected to exercise a significant influence on the observations of the $\beta_o \rightarrow \gamma$ phase transformation in the present work.

In the β-homogenised condition, i.e. at the beginning of the heating experiment, no γ reflections can be observed in the HEXRD patterns. Only above roughly 750 °C – the exact temperature depending on the reflection – intensities pertaining to the γ phase are detected by means of HEXRD (Fig. 2b). Thereupon, the γ reflections quickly increase in intensity, suggesting a rapid increase in the γ phase fraction. Based on the HEXRD signal, no evidence of the occurrence of an intermediate phase prior to the formation of γ is found.

The combination of the coarse-grained nature of the β-homogenised condition with the relatively small beam size advantageously allows collecting further structural information from the evolution of the 2D diffraction patterns. In particular, selected inter- and intra-grain relationships can be examined [38]. In Fig. 3a the evolution of a section of the diffraction pattern as marked in Fig. 2a is shown. This section contains three strong β_o reflections pertaining to the (110), (200), and (220) lattice planes. Comparing the patterns recorded at 400 °C and 700 °C, it can be observed that the β_o reflections have gained in intensity and width. Additionally, streaks have evolved around some of the β_o reflections, which extend towards selected positions on the Debye-Scherrer rings connected with the γ phase. In Fig. 3a, this finding becomes most apparent regarding the β_o-200 reflection. Further heating provokes the transfer of intensity along these streaks from β_o to γ, until at temperatures above 750 °C clear γ reflections take shape. Upon decoupling from the corresponding β_o reflections, the radial width of the reflections of both phases decreases. At 900 °C, i.e. in the final condition regarding the heating experiment, distinct γ reflections are present.

Liss et al. [38] described a similar flow of intensity along defined streaks in their seminal work on directional atomic rearrangements during the $\alpha_2 \rightarrow \gamma$ transformation in γ-TiAl based alloys. They attributed the distinct extension of the streaks to the high order and orientation relationships in the transforming regions of the grains. Similar conditions apply to the $\beta_o \rightarrow \gamma$ transformation in the present work. The azimuthal angles, at which γ reflections are formed, are initially linked to the positions of the parent β_o reflections via the orientation relationship $<111>\beta_o \{110\}\beta_o \parallel <101>\gamma \{111\}\gamma$ [10]. Based on the condition of parallel close-packed planes, this orientation relationship is documented most clearly by the formation of the γ-222 reflection in Fig. 3a. As indicated in the diffraction pattern recorded at 900 °C, γ-222 appears at exactly the same azimuthal angle as the parent β_o-220 reflection. Figure 3b allows to trace the formation of γ-222 from β_o-220 at a higher resolution. The evolution of the diffractograms, which were obtained by the azimuthal integration of a small cake segment as

indicated in the 900 °C diffraction pattern in Fig. 3a, furthermore shows that the streaking observed in the 2D patterns as well as the peak broadening and formation of peak shoulders in the 1D patterns are essentially two aspects of the same phenomenon.

A detailed analysis of the diffraction data shown in Fig. 2b reveals that first changes in the diffraction patterns can be quantified well below the onset temperature for the formation of γ reflections. Starting as early as at 550 °C, the β_o reflections distinctly gain in intensity and broaden. For example, the peak width and lattice spacing evaluated on the basis of the azimuthally integrated β_o-220 reflections are shown as a function of temperature in Fig. 3c. Starting at 550 °C, the peak width increases substantially until a maximum at 755 °C is reached. This maximum coincides with the appearance of first distinct γ reflections in the diffraction patterns, which is indicated in Fig. 3c by means of the evolution of the azimuthally integrated and summed intensities of the isolated γ-002 and γ-200 reflections. As the γ reflections increase in intensity, the β_o peak width decreases again and finally resumes the same level as in the initial β-homogenised condition. The azimuthally averaged lattice spacing of the β_o-220 reflections first increases steadily during heating as a result of thermal expansion. However, upon the onset of peak broadening, a slight drop in the rate of increase can be observed. Shortly before reaching the maximum in the peak width curve, the lattice spacing even starts to decrease, until a substantial amount of γ phase is detected by means of HEXRD. Only then, the lattice spacing again assumes a course that can be related solely to thermal expansion. This particular evolution of the lattice spacing clearly indicates changes in the chemical composition of the β_o phase. Additionally, it may be influenced by a potentially increasing degree of order in β_o.

Evidently, the onset of the $\beta_o \rightarrow \gamma$ phase transformation must be sought well below 750 °C, i.e. the temperature range in which γ is detected as a separate phase by means of HEXRD. The increase in microstrains in the β_o matrix, which is expressed by an increasing peak width

(Fig. 3c), strongly suggests the presence of submicrometre-scale particles in the early stages of growth of the γ phase.

3.3 Early stages of the γ growth sequence

3.3.1 Atomic-scale APT investigations

Two specimens were selected for the APT investigations, which were heated to either 530 °C or 680 °C at 10 $K \cdot min^{-1}$, held isothermally for 10 s, and then rapidly cooled. Thus, the first specimen (530 °C) corresponds to a condition that does not yet show any significant changes in diffraction compared to the initial β-homogenised condition. Specifically, the β_o peaks have not yet broadened (Fig. 3c). In contrast to this, the second specimen condition (680 °C) falls into the temperature range, in which already substantial peak broadening has occurred (Fig. 3c). In both conditions, no separate γ reflections are visible in the HEXRD data.

Figure 4 shows the APT reconstructions of both specimen conditions and compares them with the HEXRD and SAXS patterns at the given temperatures during the *in situ* heating experiments. In the APT reconstruction of the specimen heated to 530 °C (Fig. 4a), in which only Ti atoms are indicated for reasons of clarity, all elements appear regularly distributed. No clustering or phase separation is visually discernible. Statistical analysis based on the calculation of the nearest neighbour distribution supports the observation that long-range diffusion has not yet taken place (for details on the method please refer to a recent review by Cairney et al. [39]). This finding of a chemically homogeneous, supersaturated β_o matrix is in accordance with the HEXRD pattern that has remained unchanged compared to the initial condition (compare Figs. 2a and 4b). Visually, the 2D SAXS pattern (Fig. 4c) has not changed compared to the initial pattern at 25 °C (not shown due to the same appearance). The scattering at small *q*, i.e. around the beamstop in the centre of the image, was found to remain constant during the entire heating experiments. It can, therefore, be considered as a secondary

scattering contribution, which stems from large inhomogeneities, such as α_2 laths, grain boundaries, or impurities.

Heating to 680 °C provoked the precipitation of fine second-phase particles. In the corresponding APT reconstruction (Fig. 4d), Mo/TiO isoconcentration surfaces allow the visualisation of these precipitates. The chemical species Mo is particularly well suited for this purpose, since it strongly favours the β_o phase [34,40]. Oxygen, on the other hand, favours γ [34,40] and is in the case of the experimental conditions used during the APT measurements preferentially detected in the form of TiO. Thus, for a clear visualisation of the newly formed γ phase, the ratio of these strongly partitioning chemical species provides particularly well defined interfaces and supports the visibility of the precipitates. Figure 4d shows that the formed particles adopt the shape of discs, which is the equilibrium shape for partially coherent precipitates [41]. The discs, which have clear-cut surfaces, are oriented in a regular manner, suggesting the existence of preferred lattice planes for precipitate growth. Furthermore, the discs appear homogeneously distributed throughout the matrix. The analysis of the chemical composition of the matrix and the precipitates yielded a matrix composition of 49.9Ti-43.4Al-6.7Mo (at.%) and a precipitate composition of 51.2Ti-44.9Al-3.9Mo (at.%). The fact that both compositions lie below the nominal composition may be explained by chemical fluctuations in the sample. These findings point to the conclusion that the formed particles correspond to γ, since in accordance with literature the particle interior exhibits a reduced amount of Mo and an increased amount of Ti compared to the β_o matrix [15,20]. After heating to 680 °C at 10 $K \cdot min^{-1}$, roughly 8 to 10 vol.% of the β_o matrix have transformed to γ.

Based on the APT data, also the mean dimensions of the γ particles in the probed volume can be estimated. After heating to 680 °C, the discs were found to exhibit a mean diameter of 12.3 ± 3.9 nm and a mean thickness of 4.6 ± 0.9 nm. Thus, the mean aspect ratio μ amounts to roughly 0.37. As the discs on average consist of only some tens of unit cells in the axial direction, their scattering volume may indeed be too small as to give rise to distinct reflections

in diffraction (Fig. 4e). This finding confirms the assumptions made in section 3.2. However, due to their different chemical composition compared to the β_o matrix and their large number, the γ precipitates can be detected and investigated in an *in situ* manner by means of SAXS (Fig. 4f).

3.3.2 In situ SAXS investigations

In Fig. 5, selected 2D SAXS patterns illustrate the evolution of the SAXS signal during the *in situ* heating experiment. At 550 °C, a broad yet weak ring can be visually discerned in addition to the scattering at small q as described in section 3.3.1. While the secondary scattering contribution at small q remains constant during further heating, the diameter of the surrounding ring decreases. Simultaneously, an increase in intensity can be observed. These two findings are characteristic of particle growth.

During heating, also the shape of the scattering contours appears to change slightly (Fig. 5). At first, a circular shape is observed. The rapid increase in intensity between 600 °C and 625 °C is attended by a change towards a more radiating scattering contour, though, which becomes sharper while approaching 900 °C. Changes in scattering contours may be connected with a change in the shape of the particles during their early growth stages [42]. Additionally, anisotropic scattering contours may suggest the presence of preferred orientations of the γ precipitates with regard to the coarse-grained β_o matrix. Two weak maxima are observed on the scattering ring at 575 °C, indicating a preferred orientation of the disc-shaped precipitates. This finding is in accordance with previous studies [10,23] as well as the SEM, HEXRD, and APT results in the present work, which provide evidence of the distinct orientation relationship between β_o and γ.

For the quantitative analysis of the SAXS data, the 2D patterns were azimuthally averaged. Figure 6a shows the evolution of the integrated intensity Q' as a function of temperature. Q' is proportional to the product of the precipitate volume fraction f and the scattering contrast $\Delta\eta$ between the matrix and the precipitates. Particle growth is, therefore, reflected in a rise in Q',

as are diffusional processes that lead to an increase in $\Delta\eta$. Using Q' as a first indicator, Fig. 6a provides clear evidence for both processes within a temperature range of roughly 450 °C to 735 °C. At 735 °C, an artificial drop in the evolution of Q' is observed. This drop stems from the fact that at 735 °C the growing γ precipitates reach sizes too large to be probed by means of the employed SAXS setup, i.e. an increasing amount of their scattering signal shifts to q values without the integration limits of 0.1 to 2 nm^{-1}. The open circles in Fig. 6a, thus, represent the results for Q', which gradually diverge from Q, and illustrate, for reasons of completeness, systematic limitations in the present case.

At the same time, Fig. 6a also illustrates a significant advantage of the SAXS technique. As a result of the transmission geometry, the probed volume of the specimens is large, especially when compared to the APT measurements. Since SAXS is particularly sensitive to chemical inhomogeneities, excellent grain statistics allow to visualise even minute changes in the specimens. The evolution of Q' clearly shows that during heating first chemical changes occur already at roughly 450 °C. The low intensity values do not permit to visually observe these early processes in the 2D SAXS patterns (Fig. 4c), and the connected sub-nanometre particle sizes fall below the detection efficiency of the atom probe (see section 2.3). Starting at roughly 600 °C, Q' shows a particularly strong increase at a much accelerated rate. Basically, this change in the rate of increase could be due to two reasons. First, the precipitate growth rate could change around 600 °C. Secondly, the scattering contrast could change in this temperature range. While there appears to be no satisfactory explanation for such a prompt change in the growth rate, this finding may be rationalised on the basis of the different activation energies for the diffusion of Al and Mo (see section 4.1) [43].

Figure 6b shows selected scattering curves as obtained by the azimuthal integration of the 2D SAXS patterns. The increase in intensity and shift of the curves towards smaller q reflect the growth of the γ precipitates during heating. For a quantitative analysis of the size distributions of the γ particles, the scattering curves were fitted. Firstly, the particles were

modelled as spheres in order to avoid the introduction of assumptions on their aspect ratio or potentially changing shape during heating. These fits yielded the volume distributions of the radius R_{eq} of equivalent spheres. For the sake of comparison, the scattering curves in Fig. 6b were annotated with the peak values R_{eq} of the corresponding volume distributions. While the γ precipitates grow with increasing temperature, their size remains on the nanometre-scale over a large temperature range. In contrast, the scattering curve determined at 900 °C, which is depicted in the background of Fig. 6b, underlines the conclusion drawn above that upon exceeding roughly 735 °C the *q*-range is insufficient to analyse larger precipitates based on the SAXS signal. The characteristic features of the curves have shifted from the probed *q*-window, allowing only rough estimates of the size distributions. The complete evolution of the peak R_{eq} values is shown in Fig. 6a. Until 735 °C, the particle sizes can be determined with high accuracy. Above, the scatter in the data increases considerably, and the resulting evolution of R_{eq} artificially diverges from its smooth course. It should be noted that the sharp increase in Q' upon reaching 600 °C is not reflected in the R_{eq} values. This finding hints at a changing scattering contrast $\Delta\eta$.

In order to critically assess the validity and significance of the previous fits, the scattering curve recorded at 680 °C was fitted modelling the γ particles as spheres and as prolate ellipsoids of revolution (axes $2R_0$ and $2\mu R_0$), taking into account the results from the APT measurements (Fig. 6c). An aspect ratio μ of 0.37 was selected, and the scattering contrast $\Delta\eta$, which was, in a first approximation, set constant for the previous fits, was also calculated on the basis of the chemical compositions determined by means of APT. Figure 6c shows that both fits agree well with the SAXS data. Comparing the fits, only minor deviations can be observed in the lower *q* range. Figure 6d illustrates the volume particle size distributions corresponding to both fits. For a direct comparison with the particle dimensions obtained by means of APT, the distributions of the diameters $2R_{eq}$ and $2R_0$ are shown as well as the distribution of the discs' thickness $2\mu R_0$. The peak value $2R_{eq}$ (11.8 ± 0.1 nm) lies between

$2R_0$ (18.8 ± 0.1 nm) and $2\mu R_0$ (6.9 ± 0.1 nm). Since modelling with spheres is less time-consuming and does not require further assumptions on the particle shape, R_{eq} can be used as an efficient indicator for the kinetics of γ precipitate growth.

Finally, the obtained volume size distributions can be compared with the particle dimensions estimated on the basis of the APT data for 680 °C (mean diameter 12.3 ± 3.9 nm, mean thickness 4.6 ± 0.9 nm). While the latter dimensions clearly fall within the corresponding size distributions obtained by means of SAXS (Fig. 6d), they appear rather low compared with the peak values $2R_0$ = 18.8 ± 0.1 nm and $2\mu R_0$ = 6.9 ± 0.1 nm or with the even slightly larger average values of the volume size distributions. The reason for these deviations is likely to be found in the different grain statistics pertaining to both characterisation techniques. While SAXS probes a large number of grains, APT is restricted to considerably smaller areas and only few precipitates. Furthermore, diverse specimens were investigated. Small chemical inhomogeneities or deviations in the temperature profile may also explain different average values. Nevertheless, the overall agreement between the obtained values, especially in terms of order of magnitude, can be regarded as satisfactory.

4. Discussion

4.1 Structural considerations and the role of diffusion

The results outlined in the preceding section allow to characterise the initial β-homogenised condition as B2-structured matrix (Fig. 2), which consists of large and strongly supersaturated β_o grains (Fig. 1b). In accordance with Refs. [8,10], WQ is, thus, capable of preventing large-scale phase transformations in the Ti-44Al-7Mo (at.%) alloy. The $\beta \rightarrow \beta_o$ order transformation, though, cannot be suppressed. For near-equilibrium conditions, it occurs at 1265 °C [22]. The finding of the supersaturation and chemical homogeneity of the matrix is supported by APT and SAXS on both a local and a far-ranging scale. While in the

β-homogenised specimens some occasional larger structures are present (see section 3.3.2), some of which may be identified as α_2 laths (see sections 3.1 and 3.2), there is no evidence of the presence of γ. However, as a result of the strong supersaturation of the matrix due to the WQ from 1450 °C, a powerful driving force for the precipitation of equilibrium γ phase can be anticipated.

Based on the HEXRD results (section 3.2) it is tempting to speculate that similarly to Refs. [6,15,24,29] the $\beta_o \rightarrow \gamma$ phase transformation takes place without the formation of an intermediate phase of different crystallographic structure. This assumption is plausible, since the transformation of β_o into the structurally related γ phase can be described by a bi-axial compression along the [100] and [010] directions and an elongation along [001] as set out by Holec et al. [44]. Figure 7 illustrates the relationship between the Ti and Al sublattices of both phases based on the parent B2 structure prior to deformation. Strictly speaking, this relationship, i.e. the equivalence of the sublattices in terms of chemical species, is applicable only to stoichiometric TiAl consisting of 50 at.% Ti and 50 at.% Al. Since during WQ of the Ti-44Al-7Mo (at.%) alloy β_o does not transform spontaneously to equilibrium γ as suggested for stoichiometric TiAl [44], the addition of 7 at.% Mo undoubtedly introduces a discrete activation energy barrier to the $\beta_o \rightarrow \gamma$ phase transformation. This energy barrier stabilises β_o at room temperature. Upon heating, though, it can be overcome by means of thermal activation. A similar effect, i.e. the prevention of a spontaneous tetragonalisation of the B2 structure by means of alloying additions, has been described recently for Nb-bearing γ-TiAl based alloys [45].

The central role of diffusion can be rationalised by considering that for the formation of equilibrium γ phase (i) Mo atoms have to change from the Al sublattice in β_o to the Ti sublattice in γ due to energetic reasons [46], and (ii) element partitioning between the phases must take place [40]. In this regard, it is also not surprising that the chemical compositions of the γ precipitates (51.2Ti-44.9Al-3.9Mo (at.%)) and the β_o matrix (49.9Ti-

43.4Al-6.7Mo (at.%)) as determined by means of APT on specimens heated to 680 °C do not yet perfectly match the compositions evaluated on long-term annealed specimens (γ: 47.4Ti-50.6Al-2.0Mo (at.%), β_o: 48.4Ti-34.8Al-16.3Mo (at.%) [10]). As a consequence, it can be concluded that in the course of the proposed two-step heat treatment the diffusional growth of γ precipitates is controlled by elemental redistribution rather than interface migration.

Compared to Al and Ti, Mo appears to be a slower diffuser in the B2 structure [47]. Specifically, the activation energy of Mo for short distance diffusion is higher than the self-diffusion energies for Ti and Al [43,48]. Due to the changing circumstances during continuous heating, this fact complicates the description of γ precipitate growth. Based on the SAXS results, and in particular the evolution of Q' (Fig. 6a), it could be argued that the diffusional growth below 600 °C is largely driven by Al diffusion. As a result of the sub-nanometre-scale precipitate sizes and the short-ranged nature of the diffusional processes, this growth stage cannot be probed easily by means of APT (Fig. 4a), while based on excellent grain statistics SAXS already yields a weak signal. Above 600 °C, Mo diffusion sets in, as proven by the APT measurements (Fig. 4d). The sudden onset of Mo partitioning may yield a much stronger scattering contrast $\Delta\eta$ and a sharp increase in Q' as observed in Fig. 6a.

Based on this explanation, it must be assumed that during the heating experiment both the scattering contrast $\Delta\eta$ and the precipitate volume fraction f change. In combination with the assumed change in particle shape based on the analysis of the scattering contours (Fig. 5), it appears sensible to confine a first analysis of the SAXS data to a simple model. This paper, for example, uses the radius R_{eq} of equivalent spheres to trace the growth kinetics of the γ precipitates. For the fits, which were shown to yield significant results in the temperature range of 450 °C to 735 °C, $\Delta\eta$ was set constant. Consequently, the volume fraction is not reported.

4.2 Distinguishing characteristics of the γ precipitates and their implications

The characterisation of the γ precipitates in their early growth stages revealed several striking features. Firstly, the γ particles appear distributed homogenously throughout the β_o matrix (Figs. 1c, 1d, and 4d). Secondly, the particles possess clear-cut surfaces, similarly to the γ particles formed upon annealing in Nb-bearing alloys [29]. Hence, an eventual network structure as described in Ref. [23] must be formed during later growth stages. Thirdly, there exists a distinct orientation relationship between γ and β_o as proposed in Ref. [10], which is reflected in the arrangement of axes in the SEM images (Figs. 1c and d), the azimuthal angle positions and streaks in the 2D HEXRD patterns (Fig. 3a), the regular orientation of the discs as observed in the APT reconstructions (Fig. 4d), and in the radiating shape of the SAXS signal (Fig. 5). Although the present work clearly focuses on the growth of γ precipitates, some general conclusions about the $\beta_o \rightarrow \gamma$ phase transformation may be drawn from these findings.

The homogeneous distribution of the γ particles points to the presence of a substantial number of rather homogeneously distributed, potential nucleation sites in the β-homogenised condition. Indeed, literature suggests the existence of a high density of stacking faults [10] and a considerable number of excess out-of-equilibrium vacancies frozen during WQ [43]. These faults in the β_o matrix lattice are likely to assist the heterogeneous nucleation of the γ particles and, upon heating, to increase diffusion rates. These considerations are based on the implicit understanding that the observed phase transformation can be described as a nucleation and growth process. However, the comparison between the chemical compositions of the γ precipitates after heating to 680 °C and after annealing at 1000 °C for 168 h already shows that the conditions of classic nucleation are not ideally fulfilled [41]: the early γ precipitates do not yet exhibit their equilibrium composition. In short, the discussion of the observed $\beta_o \rightarrow \gamma$ phase transformation is a delicate issue. The primary cause for its

complexity can be found in the applied two-step heat treatment, which encompasses quenching and heating segments, i.e. varying conditions regarding diffusion. As quenched B2 structures often exhibit anomalies unexpected for purely diffusional transformations [49–51], the earliest stages of the $\beta_o \rightarrow \gamma$ phase transformation will be treated in a forthcoming publication using dedicated methods. While the present work focuses on diffusional growth, it should be noted, though, that the results from the HEXRD, APT, and SAXS investigations make a strong case for a nucleation and growth process as opposed to, e.g., spinodal decomposition.

Firstly, they show that the formed particles are not interconnected and possess clear-cut interfaces during the early stages of growth [52,53]. Secondly, for a spinodal decomposition to occur, a spontaneous and barrier-free transformation path is required [41]. While this seems to be the case for stoichiometric γ-TiAl [44], a discrete activation energy barrier is to be expected in the Ti-44Al-7Mo (at.%) alloy as set out above. Finally, in accordance with Refs. [10,23,29], a distinct orientation relationship is observed between the ordered B2 matrix and the γ precipitates. Typically, spinodal decomposition is described to occur in the course of the precipitation of an ordered phase from a disordered matrix [53]. The establishment of an orientation relationship between two ordered phases via spinodal decomposition, i.e. a structural rearrangement following changes in the chemical composition, appears much less likely than a diffusional compensation following the adjustment of the crystal structure. This is especially true in the present case, in which the basic adjustment of the crystal structure requires only the compression or elongation of certain unit cell axes.

4.3 Growth of the γ precipitates

Figure 8 summarises the key results of the *in situ* heating experiments in the shape of one graphical representation. It combines the evolution of the β_o peak width and summed intensity of the γ-002 and γ-200 peaks as determined by means of HEXRD (section 3.2) with the *in situ*

SAXS results (section 3.3.2), i.e. the evolution of the integrated intensity Q' and the radius R_{eq} of equivalent spheres. Evidently, the *in situ* techniques used in this work complement each other. As indicated at the top of Fig. 8, the strength of HEXRD lies in the higher temperature regime, in which the γ precipitates can be structurally characterised due to their sufficient size and scattering volume. In a broader sense, the area of application of HEXRD extends to lower temperatures, at which indications are provided as to the processes taking place in the β_o matrix lattice. Supported by APT, a local yet direct imaging technique, *in situ* SAXS proved applicable to the lower temperature regime, which is limited by the probed *q*-range. The considerable asset of SAXS can be found in its sensitivity to even minute compositional changes, which results from the large volume examined in transmission geometry. In this way, the onset of first diffusional processes can be determined, extending the field of view to very early growth stages.

Based on the results of HEXRD, APT, and SAXS (Fig. 8), it can be concluded that first processes that can be ascribed to the thermally activated growth of γ set in at a temperature of roughly 450 °C. The first particles that become apparent from the SAXS patterns possess an equivalent radius R_{eq} in the sub-nanometre range. As for their formation, thus, only short-range reordering between few lattice planes is necessary, and the diffusional processes are likely to be still confined to Al and Ti atoms as opposed to Mo, these minute changes are not reflected in the APT data.

Upon further heating, the precipitates grow (Fig. 8). It can be assumed that the small particles at first possess coherent interfaces with the β_o matrix. During growth, the matrix lattice is thus increasingly strained, as for the formation of γ a lattice deformation as described in section 4.1 is necessary and the $<111>\beta_o$ $\{110\}\beta_o \parallel <101>\gamma$ $\{111\}\gamma$ orientation relationship cannot provide a perfect match between the B2 and $L1_0$ lattices extending over large areas [41]. The microstrains in the β_o matrix, which result from the misfit-induced strain fields around the γ precipitates, are expressed by the broadening of the β_o reflections as observed by

means of HEXRD [54]. Figure 8 shows, for example, the increase in β_o-220 peak width above temperatures of roughly 550 °C. In this temperature range, the γ particles must already be sufficiently large to exercise a certain level of strain. As can be seen from the evolution of R_{eq}, they possess an equivalent radius R_{eq} exceeding 2 nm. At 680 °C, the β_o-220 peak width has substantially increased. The disc-shaped γ precipitates, whose existence is unambiguously proved by the *ex situ* APT measurements, are still not detected directly by means of HEXRD. Due to their nanometre-scale dimensions, as determined from both APT and SAXS, their scattering volume may be too small. However, streaks have evolved around the β_o reflections testifying to the transfer of intensity from β_o to γ.

Heating leads to a further increase in microstrains in the β_o matrix, until it becomes energetically favourable to forego the coherent interface. For the $<111>\beta_o$ $\{110\}\beta_o \parallel <101>\gamma$ $\{111\}\gamma$ orientation relationship in particular, a good fit is typically restricted to small diamond-shaped areas [41]. Consequently, the growth of γ precipitates must necessitate the loss of coherency at some point. At this tipping point, which is suggested to occur at about 755 °C (Fig. 8), the peak broadening and, thus, the microstrains start to decrease. Combined with the change in the β_o-220 lattice spacing as set out in section 3.2, these findings point to a proceeding phase separation and relaxation of the matrix lattice [52].

Above 750 °C, the γ precipitates have acquired a sufficient volume and show in the HEXRD patterns as distinct reflections. The γ reflections have decoupled from the matrix reflections, and streaks have vanished. The fine-grained nature and large number of γ particles are reflected in the HEXRD patterns by a distinct mosaic spread. Based on their small grain size, it can be expected that the γ precipitates still exhibit semi-coherent interfaces with the β_o matrix, as described in Refs. [29,55]. Further heating or ensuing isothermal annealing below the eutectoid temperature leads to a coarsening of the γ precipitates. However, it was shown that even after 100 h at 900 °C the dimensions of the precipitates remain on the

submicrometre-scale (Fig. 1), giving rise to a homogeneous and refined microstructure that can be adjusted solely via heat treatments without the need for prior hot working.

5. Conclusions

The addition of β-stabilising elements to γ-TiAl based alloys entails novel opportunities in microstructural design. In this context, the present work examines the growth behaviour of γ precipitates from a β_o matrix in a β-homogenised Ti-44Al-7Mo (at.%) alloy. *In situ* diffraction (HEXRD) and scattering (SAXS) techniques were combined with a direct imaging technique (APT) to address for the first time the early stages of the γ growth sequence in high-Mo containing γ-TiAl based alloys. Based on the results, the following conclusions can be drawn:

- The $\beta_o \rightarrow \gamma$ phase transformation seems to take place without the formation of an intermediate phase of different crystallographic structure. The addition of 7 at.% Mo compared to stoichiometric TiAl stabilises β_o at room temperature and introduces a discrete activation energy barrier to the $\beta_o \rightarrow \gamma$ phase transformation.
- At a heating rate of 10 $K \cdot min^{-1}$, first diffusional processes that can be ascribed to the $\beta_o \rightarrow \gamma$ phase transformation set in at roughly 450 °C. The growth of the γ precipitates is controlled by elemental redistribution. Furthermore, it is connected with the introduction of misfit-induced strain fields around the initially coherent γ precipitates, which upon further heating result in the loss of coherency between the disc-shaped γ particles and the β_o matrix.
- Continuous heating is connected not only with a changing precipitate volume fraction, but also with a changing scattering contrast. A simple model based on equivalent spheres proved an efficient means to trace the growth kinetics of the γ particles from the SAXS data.

- The findings discussed in this paper not only deepen the present understanding of the $\beta_o \rightarrow \gamma$ phase transformation in γ-TiAl based alloys. They also provide quantitative data, which represent an essential prerequisite for the design of refined microstructures in β-stabilised γ-TiAl based alloys without the need for prior hot working.

Acknowledgements

P. Erdely is a recipient of a DOC Fellowship of the Austrian Academy of Sciences at the Department of Physical Metallurgy and Materials Testing, Montanuniversität Leoben. The authors thank Dr. V. Güther, GfE Metalle und Materialien GmbH, for providing the γ-TiAl based ingot material. With regard to the *in situ* diffraction and scattering experiments, the support of the DESY management and user office is gratefully acknowledged. We appreciate the commitment of the HZG beamline staff who contributed greatly to the success of the experiments performed.

References

[1] F. Appel, J.D.H. Paul, M. Oehring, Gamma titanium aluminide alloys - Science and technology, Wiley-VCH Verlag & Co. KGaA, Weinheim, Germany, 2011.

[2] T. Tetsui, K. Shindo, S. Kobayashi, M. Takeyama, A newly developed hot worked TiAl alloy for blades and structural components, Scr. Mater. 47 (2002) 399–403. doi:10.1016/S1359-6462(02)00158-6.

[3] M. Takeyama, S. Kobayashi, Physical metallurgy for wrought gamma titanium aluminides: Microstructure control through phase transformations, Intermetallics 13 (2005) 993–999. doi:10.1016/j.intermet.2004.12.014.

[4] H. Clemens, W. Wallgram, S. Kremmer, V. Güther, A. Otto, A. Bartels, Design of novel β-solidifying TiAl alloys with adjustable β/B2-phase fraction and excellent hot-workability, Adv. Eng. Mater. 10 (2008) 707–713. doi:10.1002/adem.200800164.

[5] S. Mayer, P. Erdely, F.D. Fischer, D. Holec, M. Kastenhuber, T. Klein, H. Clemens, Intermetallic β-solidifying γ-TiAl based alloys − From fundamental research to application, Adv. Eng. Mater. 19 (2017) 1–27. doi:10.1002/adem.201600735.

[6] T.T. Cheng, M.H. Loretto, The decomposition of the beta phase in Ti-44Al-8Nb and Ti-44Al-4Nb-4Zr-0.2Si alloys, Acta Mater. 46 (1998) 4801–4819. doi:10.1016/S1359-6454(98)00113-X.

[7] F. Appel, M. Oehring, J.D.H. Paul, Nano-scale design of TiAl alloys based on β-phase decomposition, Adv. Eng. Mater. 8 (2006) 371–376.

[8] S. Mayer, C. Sailer, T. Schmoelzer, H. Clemens, T. Lippmann, P. Staron, V. Güther, M. Takeyama, On phase equilibria and phase transformations in β/γ-TiAl alloys - A short review, BHM Berg- Und Hüttenmännische Monatshefte 156 (2011) 438–442. doi:10.1007/s00501-011-0033-0.

[9] H. Clemens, S. Mayer, Design, processing, microstructure, properties, and applications of

advanced intermetallic TiAl alloys, Adv. Eng. Mater. 15 (2013) 191–215. doi:10.1002/adem.201200231.
[10] B. Rashkova, K. Spiradek-Hahn, M. Brabetz, Z. Zhang, T. Schöberl, H. Clemens, S. Mayer, Microstructural evolution and grain refinement in an intermetallic titanium aluminide alloy with a high molybdenum content, Int. J. Mater. Res. 106 (2015) 725–731. doi:10.3139/146.111235.
[11] M. Kimura, K. Hashimoto, H. Morikawa, Study on phase stability in Ti-Al-X systems at high temperatures, Mater. Sci. Eng. A 152 (1992) 54–59. doi:10.1016/0921-5093(92)90046-4.
[12] M. Kimura, K. Hashimoto, High-temperature phase equilibria in Ti-Al-Mo system, J. Phase Equilibria 20 (1999) 224–230. doi:10.1361/105497199770335758.
[13] R. Kainuma, Y. Fujita, H. Mitsui, I. Ohnuma, K. Ishida, Phase equilibria among α (hcp), β (bcc) and γ ($L1_0$) phases in Ti-Al base ternary alloys, Intermetallics 8 (2000) 855–867. doi:16/S0966-9795(00)00015-7.
[14] Y.G. Li, M.H. Loretto, Microstructure and fracture behaviour of Ti-44Al-xM derivatives, Acta Metall. 42 (1994) 2913–2919. doi:10.1016/0956-7151(94)90388-3.
[15] A.K. Singh, D. Banerjee, Transformation in α_2+γ titanium aluminide alloys containing molybdenum: Part I. Solidification behavior, Metall. Mater. Trans. A 28 (1997) 1735–1743. doi:doi.org/10.1007/s11661-997-0105-7.
[16] R. Kainuma, I. Ohnuma, K. Ishikawa, K. Ishida, Stability of B2 ordered phase in the Ti-rich portion of Ti-Al-Cr and Ti-Al-Fe ternary systems, Intermetallics 8 (2000) 2–8. doi:10.1016/S0966-9795(00)00016-9.
[17] S. Azad, R.K. Mandal, A.K. Singh, Effect of Mo addition on transformation behavior of (α_2+γ) based Ti-Al alloys, Mater. Sci. Eng. A 429 (2006) 219–224. doi:10.1016/j.msea.2006.05.077.
[18] D.M. Cupid, O. Fabrichnaya, F. Ebrahimi, H.J. Seifert, Thermodynamic assessment of the Al-Mo system and of the Ti-Al-Mo System from 0 to 20 at.% Ti, Intermetallics 18 (2010) 1185–1196. doi:10.1016/j.intermet.2010.03.010.
[19] S. Mayer, C. Sailer, H. Nakashima, T. Schmoelzer, T. Lippmann, P. Staron, K.-D. Liss, H. Clemens, M. Takeyama, Phase equilibria and phase transformations in molybdenum-containing TiAl alloys, in: Mater. Res. Soc. Symp. Proc., Warrendale, PA, USA, 2011: pp. 113–118. doi:10.1557/opl.2011.31.
[20] V.T. Witusiewicz, A.A. Bondar, U. Hecht, O.M. Stryzhyboroda, N.I. Tsyganenko, V.M. Voblikov, V.M. Petyukh, T.Ya. Velikanova, Thermodynamic re-modelling of the ternary Al–Mo–Ti system based on novel experimental data, J. Alloys Compd. 749 (2018) 1071–1091. doi:10.1016/j.jallcom.2018.03.283.
[21] T. Schmoelzer, S. Mayer, C. Sailer, F. Haupt, V. Güther, P. Staron, K.-D. Liss, H. Clemens, In situ diffraction experiments for the investigation of phase fractions and ordering temperatures in Ti - 44 at%Al - (3-7) at%Mo alloys, Adv. Eng. Mater. 13 (2011) 306–311. doi:10.1002/adem.201000263.
[22] S. Kabra, K. Yan, S. Mayer, T. Schmoelzer, M. Reid, R. Dippenaar, H. Clemens, K.-D. Liss, Phase transition and ordering behavior of ternary Ti-Al-Mo alloys using in-situ neutron diffraction, Int. J. Mater. Res. 102 (2011) 697–702. doi:10.3139/146.110528.
[23] M. Engstler, S. Mayer, C. Pauly, H. Clemens, F. Mücklich, 3D characterization of an intermetallic β/γ-titanium aluminide alloy, Adv. Eng. Mater. 15 (2013) 1125–1128. doi:10.1002/adem.201300041.
[24] A.K. Singh, D. Banerjee, Transformations in α_2+γ titanium aluminide alloys containing molybdenum: Part II. Heat treatment, Metall. Mater. Trans. A 28 (1997) 1745–1753. doi:10.1007/s11661-997-0106-6.
[25] M. Schloffer, B. Rashkova, T. Schöberl, E. Schwaighofer, Z. Zhang, H. Clemens, S. Mayer, Evolution of the ω_o phase in a β-stabilized multi-phase TiAl alloy and its effect on hardness, Acta Mater. 64 (2014) 241–252. doi:10.1016/j.actamat.2013.10.036.
[26] T. Klein, B. Rashkova, D. Holec, H. Clemens, S. Mayer, Silicon distribution and silicide precipitation during annealing in an advanced multi-phase γ-TiAl based alloy, Acta Mater. 110 (2016) 236–245. doi:10.1016/j.actamat.2016.03.050.
[27] M. Kastenhuber, T. Klein, B. Rashkova, I. Weißensteiner, H. Clemens, S. Mayer, Phase transformations in a β-solidifying γ-TiAl based alloy during rapid solidification, Intermetallics

91 (2017) 100–109. doi:10.1016/j.intermet.2017.08.017.
[28] S. Goyel, O. Rios, M.S. Kesler, F. Ebrahimi, Two-step nucleation of the γ-phase in a Ti-45Al-18Nb alloy, Intermetallics 18 (2010) 1491–1497. doi:10.1016/j.intermet.2010.03.042.
[29] L. Song, X. Hu, T. Zhang, J. Li, Precipitation behaviors in a quenched high Nb-containing TiAl alloy during annealing, Intermetallics 89 (2017) 79–85. doi:10.1016/j.intermet.2017.05.025.
[30] L. Song, J. Lin, J. Li, Phase transformation mechanisms in a quenched Ti-45Al-8.5Nb-0.2W-0.2B-0.02Y alloy after subsequent annealing at 800 °C, J. Alloys Compd. 691 (2017) 60–66. doi:10.1016/j.jallcom.2016.08.238.
[31] A.P. Hammersley, S.O. Svensson, M. Hanfland, A.N. Fitch, D. Häusermann, Two-dimensional detector software: From real detector to idealised image or two-theta scan, High Press. Res. 14 (1996) 235–248. doi:10.1080/08957959608201408.
[32] The MathWorks Inc., MATLAB and Statistics Toolbox, (2017).
[33] P. Staron, U. Christoph, F. Appel, H. Clemens, SANS investigation of precipitation hardening of two-phase γ-TiAl alloys, Appl. Phys. A Mater. Sci. Process. 75 (2002) 1–3. doi:10.1007/s003390201870.
[34] T. Klein, H. Clemens, S. Mayer, Advancement of compositional and microstructural design of intermetallic γ-TiAl based alloys determined by atom probe tomography, Materials 9 (2016) 1–19. doi:10.3390/ma9090755.
[35] M. Schloffer, T. Schmoelzer, S. Mayer, E. Schwaighofer, G. Hawranek, F.-P. Schimansky, F. Pyczak, H. Clemens, The characterisation of a powder metallurgically manufactured TNM™ titanium aluminide alloy using complimentary quantitative methods, Pract. Metallogr. 48 (2011) 594–604. doi:10.3139/147.110138.
[36] S. Das, J.M. Howe, J.H. Perepezko, A high-resolution transmission electron microscopy study of interfaces between the γ, B2 , and α_2 phases in a Ti-Al-Mo alloy, Metall. Mater. Trans. A 27 (1996) 1623–1634.
[37] M.H. Loretto, A.B. Godfrey, D. Hu, P.A. Blenkinsop, I.P. Jones, T.T. Cheng, The influence of composition and processing on the structure and properties of TiAl-based alloys, Intermetallics 6 (1998) 663–666. doi:10.1016/S0966-9795(98)00035-1.
[38] K.-D. Liss, A. Stark, A. Bartels, H. Clemens, T. Buslaps, D. Phelan, L.A. Yeoh, Directional atomic rearrangements during transformations between the α- and γ-phases in titanium aluminides, Adv. Eng. Mater. 10 (2008) 389–392. doi:10.1002/adem.200700322.
[39] J.M. Cairney, K. Rajan, D. Halye, B. Gault, P.A.J. Bagot, P.-P. Choi, P.J. Felfer, S.P. Ringer, R.K.W. Marceau, M.P. Moody, Mining information from atom probe data, Ultramicroscopy 159 (2015) 324–337. doi:10.1016/j.ultramic. 2015.05.006.
[40] T. Klein, M. Schachermayer, F. Mendez-Martin, T. Schöberl, B. Rashkova, H. Clemens, S. Mayer, Carbon distribution in multi-phase γ-TiAl based alloys and its influence on mechanical properties and phase formation, Acta Mater. 94 (2015) 205–213. doi:10.1016/j.actamat.2015.04.055.
[41] D.A. Porter, K.E. Easterling, Transformations in metals and alloys, 2nd ed., Chapman & Hall, London, UK, 1992.
[42] F. Langmayr, P. Fratzl, G. Vogl, W. Miekeley, Crossover from ω-phase to α-phase precipitation in bcc Ti-Mo, Phys. Rev. B 49 (1994) 11759–11766. doi:10.1103/PhysRevB.49.11759.
[43] L. Usategui, M.L. Nó, S. Mayer, H. Clemens, J.S. Juan, Internal friction and atomic relaxation processes in an intermetallic Mo-rich Ti-44Al-7Mo ($\gamma+\beta_o$) model alloy, Mater. Sci. Eng. A 700 (2017) 495–502. doi:10.1016/j.msea.2017.06.014.
[44] D. Holec, D. Legut, L. Isaeva, P. Souvatzis, H. Clemens, S. Mayer, Interplay between effect of Mo and chemical disorder on the stability of β/β_o-TiAl phase, Intermetallics 61 (2015) 85–90. doi:10.1016/j.intermet.2015.03.001.
[45] T. Klein, D. Holec, H. Clemens, S. Mayer, Pathways of phase transformation in β-phase-stabilized σ/γ-TiAl alloys subjected to two-step heat treatments, Scr. Mater. 149 (2018) 112–119. doi:10.1016/j.scriptamat.2018.02.009.
[46] D. Holec, R.K. Reddy, T. Klein, H. Clemens, Preferential site occupancy of alloying elements in TiAl-based phases, J. Appl. Phys. 119 (2016) 205104. doi:10.1063/1.4951009.
[47] T. Klein, M. Schachermayer, D. Holec, B. Rashkova, H. Clemens, S. Mayer, Impact of Mo on

the ω_o phase in β-solidifying TiAl alloys: An experimental and computational approach, Intermetallics 85 (2017) 26–33. doi:10.1016/j.intermet.2017.01.011.
[48] Y. Mishin, C. Herzig, Diffusion in the Ti–Al system, Acta Mater. 48 (2000) 589–623. doi:10.1016/S1359-6454(99)00400-0.
[49] R. Strychor, J.C. Williams, W.A. Soffa, Phase transformations and modulated microstructures in Ti-Al-Nb alloys, Metall. Trans. A 19 (1988) 225–234. doi:10.1007/BF02652530.
[50] S. Djanarthany, C. Servant, R. Penelle, Influence of an increasing content of molybdenum on phase transformations of Ti-Al-Mo aluminides - relation with mechanical properties, Mater. Sci. Eng. A 152 (1992) 48–53. doi:10.1016/0921-5093(92)90045-3.
[51] X. Ren, M. Hagiwara, Displacive precursor phenomena in Ti-22Al-27Nb intermetallic compound prior to diffusional transformation, Acta Mater. 49 (2001) 3971–3980. doi:10.1016/S1359-6454(01)00288-9.
[52] E. Eidenberger, M. Schober, T. Schmoelzer, E. Stergar, P. Staron, H. Leitner, H. Clemens, Analysis of the multistage phase separation reaction in Fe-25 at% Co-9at%Mo, Phys. Status Solidi A 207 (2010) 2238–2246. doi:10.1002/pssa.201026059.
[53] G.B. Viswanathan, R. Banerjee, A. Singh, S. Nag, J. Tiley, H.L. Fraser, Precipitation of ordered phases in metallic solid solutions: A synergistic clustering and ordering process, Scr. Mater. 65 (2011) 485–488. doi:10.1016/j.scriptamat.2011.06.002.
[54] F. Appel, J.D.H. Paul, P. Staron, M. Oehring, O. Kolednik, J. Predan, F.D. Fischer, The effect of residual stresses and strain reversal on the fracture toughness of TiAl alloys, Mater. Sci. Eng. A 709 (2018) 17–29. doi:10.1016/j.msea.2017.10.010.
[55] L.C. Zhang, M. Aindow, Morphology and interfacial structure of gamma precipitates in the beta phase of a Ti-Al-Nb-Zr alloy, J. Mater. Sci. 41 (2006) 611–619. doi:10.1007/s10853-006-6477-z.

Figures and figure captions

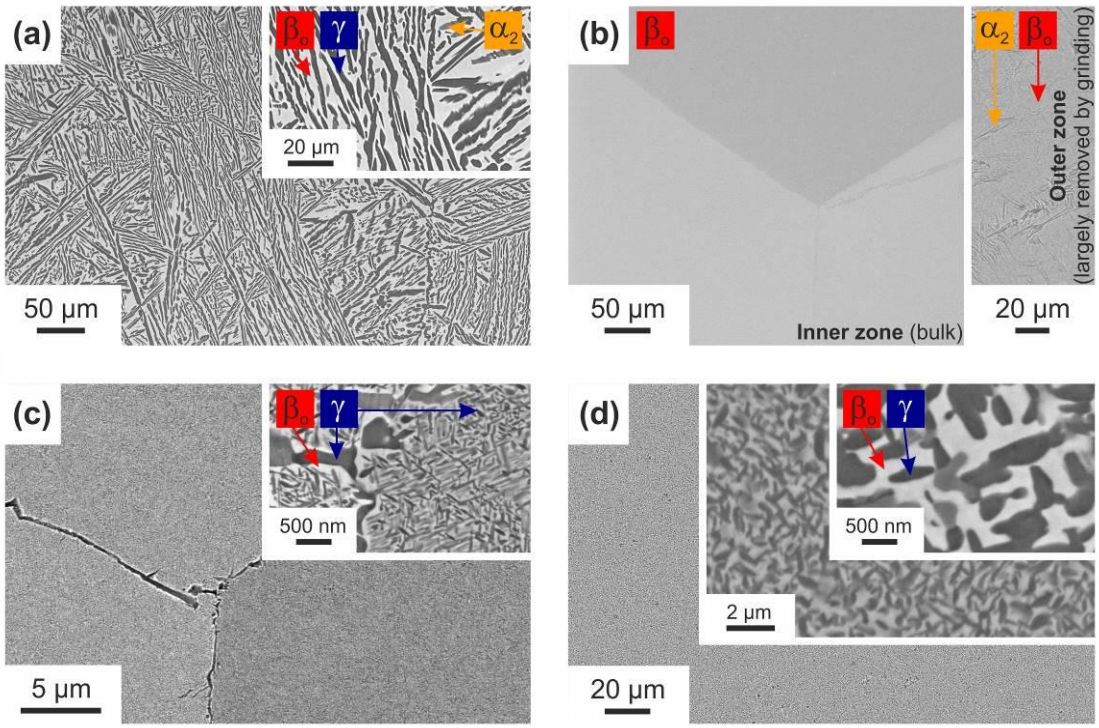

Fig. 1: SEM-BSE micrographs of the Ti-44Al-7Mo (at.%) alloy in the following conditions: (**a**) cast/HIP, (**b**) β-homogenised (1450 °C/30 min/WQ), (**c**) β-homogenised and continuously heated to 900 °C at 10 $K \cdot min^{-1}$, and (**d**) β-homogenised and isothermally annealed at 900 °C for 100 h. The inserts represent higher magnifications and include the labelling of the main microstructural features. The insert in panel (**b**) extends the view of the inner zone of the specimens, which consists of β_o grains with varying orientation contrast, to the surface-near outer zone. Note that the scales vary among the panels.

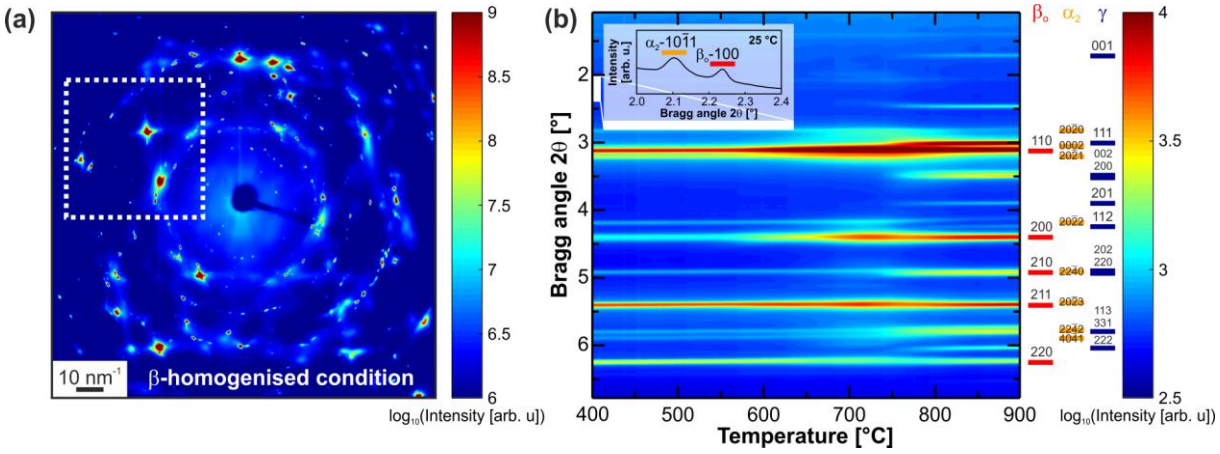

Fig. 2: Diffraction pattern (raw data) of (**a**) the β-homogenised initial condition and (**b**) evolution of the azimuthally integrated intensities during continuous heating to 900 °C at a constant rate of 10 K·min^{-1}. In panel (**a**), a section of the diffraction pattern that contains three strong β_o reflections (i.e. β_o-110, β_o-200, and β_o-220 in radial direction) is marked. To the right of panel (**b**), further selected reflections are indexed with respect to the Bragg angle 2θ. The insert at the top of panel (**b**) documents the presence of the weak β_o-100 and α_2-10$\bar{1}$1 superstructure reflections in the β-homogenised condition at 25 °C.

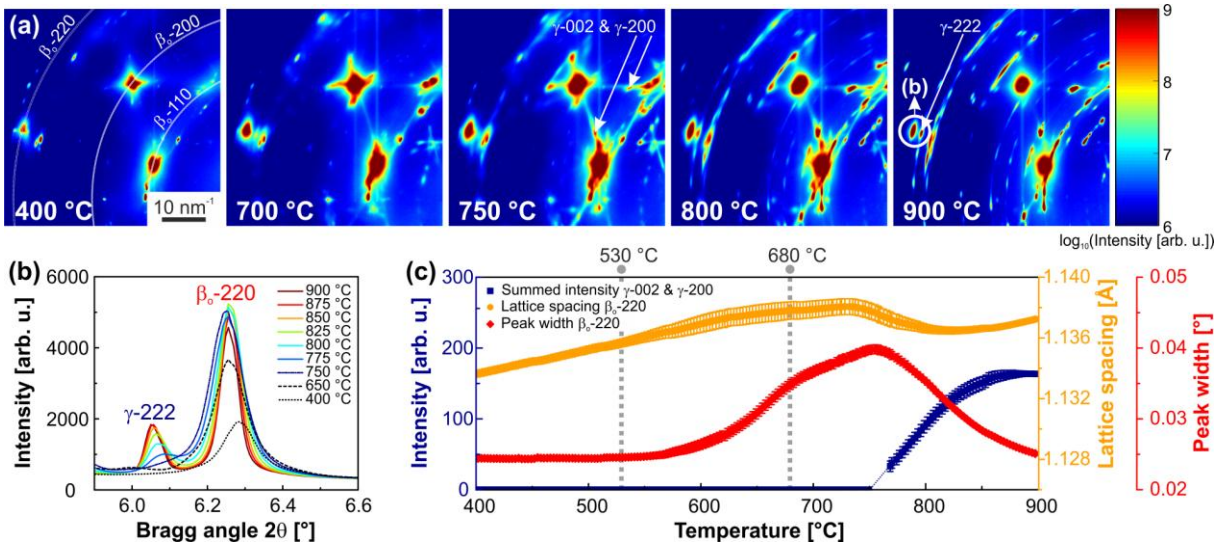

Fig. 3: Evolution of a section of the 2D diffraction pattern (as marked in Fig. 2) during (**a**) continuous heating to 900 °C at a constant rate of 10 K·min^{-1} and (**b,c**) quantitative analysis of the diffraction data. In panel (**b**), the formation of the γ-222 from the β_o-220 reflection (as marked in the last subpanel in (**a**)) is traced by means of diffractograms. Panel (**c**) displays the evolution of the lattice spacing and peak width of all β_o-220 reflections and compares these data with the summed intensity evolution of the γ-002 and γ-200 reflections. Two temperatures prior to the detection of γ phase by means of HEXRD are marked; these heat treatment conditions were chosen for the *ex situ* APT measurements (see section 3.3.1).

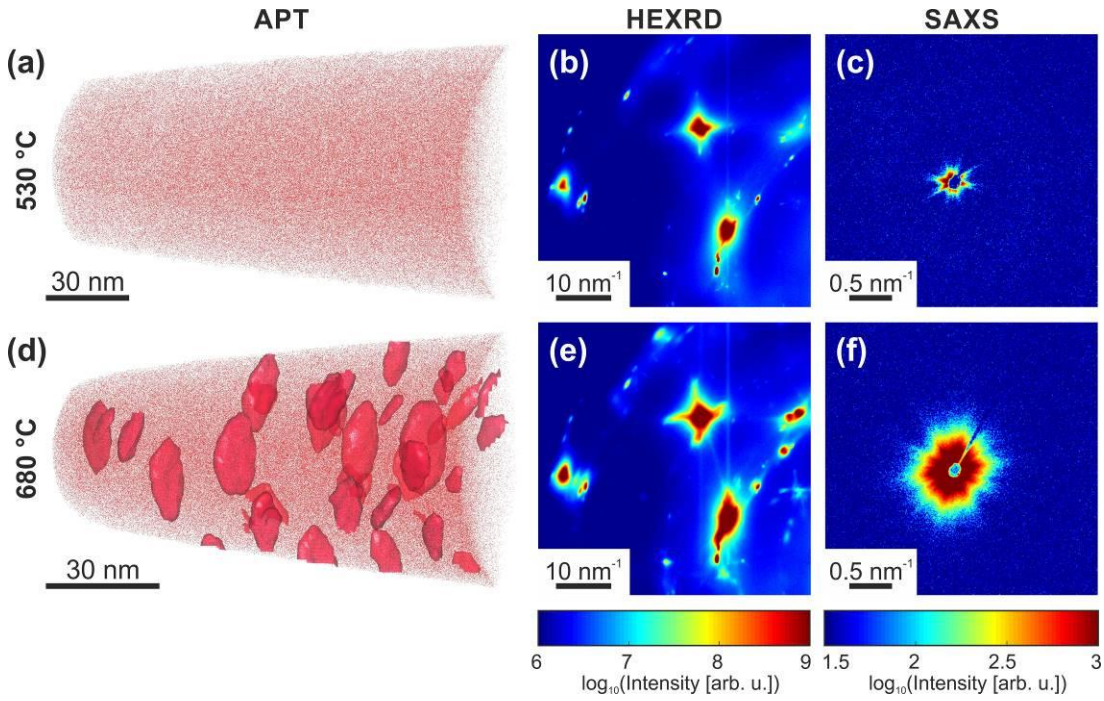

Fig. 4: Comparison of two Ti-44Al-7Mo (at.%) specimens that were heated at a constant rate of 10 $K \cdot min^{-1}$ to either 530 °C or 680 °C. For the APT measurements (**a,d**), the specimens were rapidly cooled after an isothermal segment of 10 s at the indicated temperatures. In the APT reconstructions, only Ti atoms are indicated for reasons of clarity. While in panel (**a**) no clustering or phase separation is discernible, Mo/TiO isoconcentration surfaces allow to visualise the formation of disc-shaped precipitates in (**d**).The corresponding HEXRD (**b,e**) and SAXS (**c,f**) images stem from the *in situ* heating experiments and were taken at the indicated temperatures.

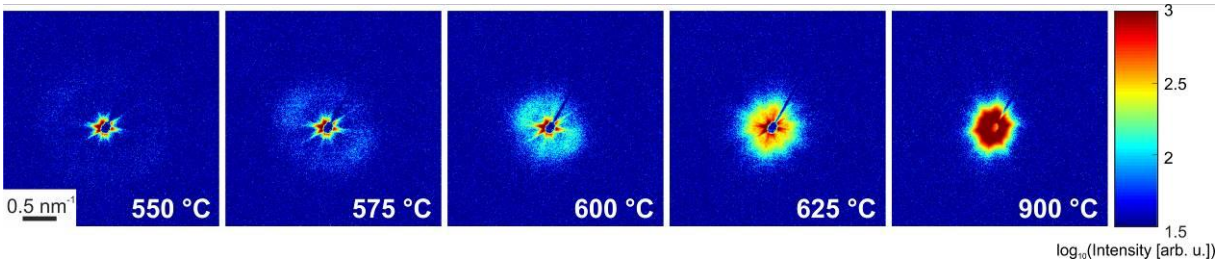

Fig. 5: Evolution of the 2D SAXS pattern (uncorrected raw data) during continuous heating to 900 °C at a constant rate of 10 K·min^{-1}. The subpanels correspond to 550, 575, 600, 625, and 900 °C, respectively.

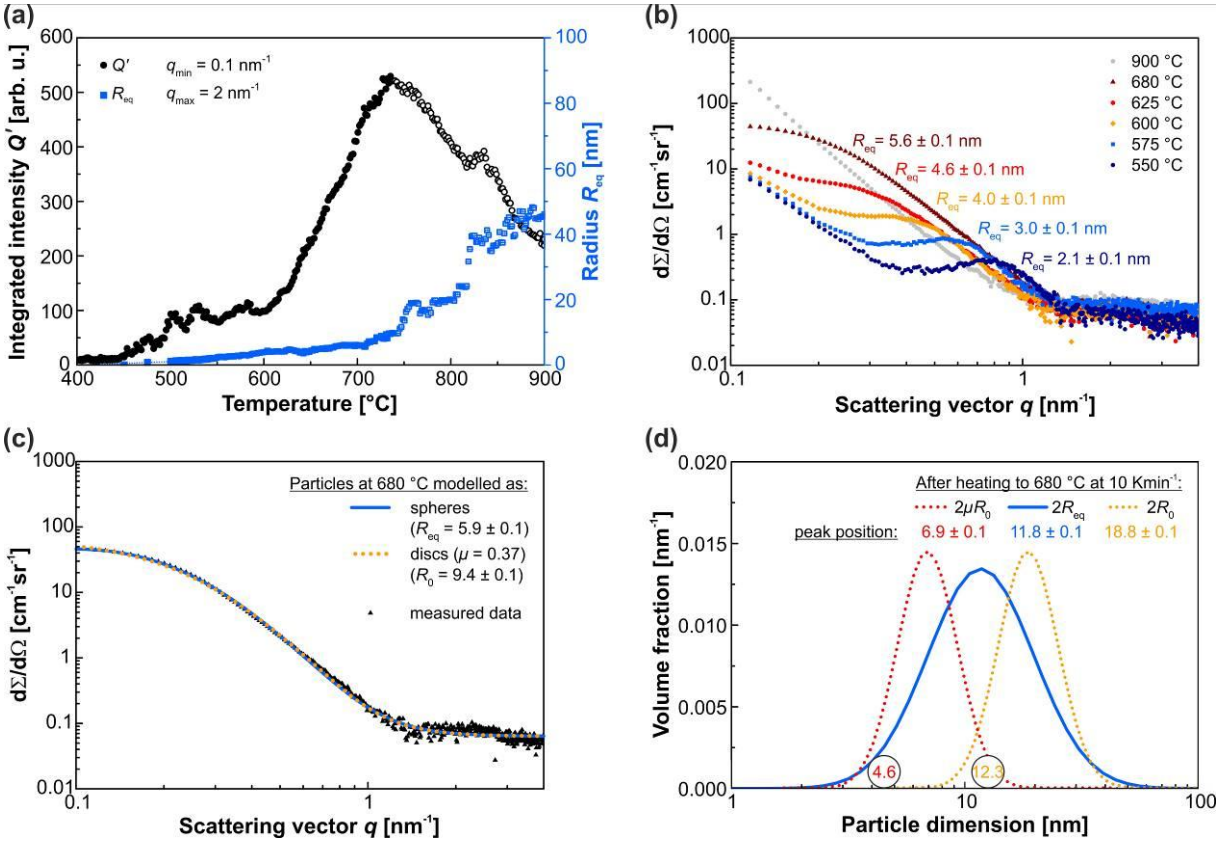

Fig. 6: Quantitative analysis of the SAXS data. Panel (**a**) shows the evolution of the integrated intensity Q' and the radius R_{eq} of equivalent spheres as a function of temperature. Full symbols represent significant data, while open symbols above 735 °C illustrate systematic limitations in the SAXS experiment due to the probed q-range of 0.1 to 2 nm^{-1} (see section 3.3.2). In panel (**b**), selected scattering curves are given, which were annotated with the peak values R_{eq} of the corresponding volume size distributions. In panel (**c**), the scattering curve measured at 680 °C is shown fitted modelling the γ particles either as spheres with a radius of R_{eq} or as prolate ellipsoids of revolution with axes of $2R_0$ and $2\mu R_0$. The corresponding precipitate volume size distributions are displayed in panel (**d**). In order to enable a direct comparison with the mean APT results, which are indicated as circles above the horizontal axis, the distributions of $2R_{eq}$, $2R_0$ and $2\mu R_0$ are shown.

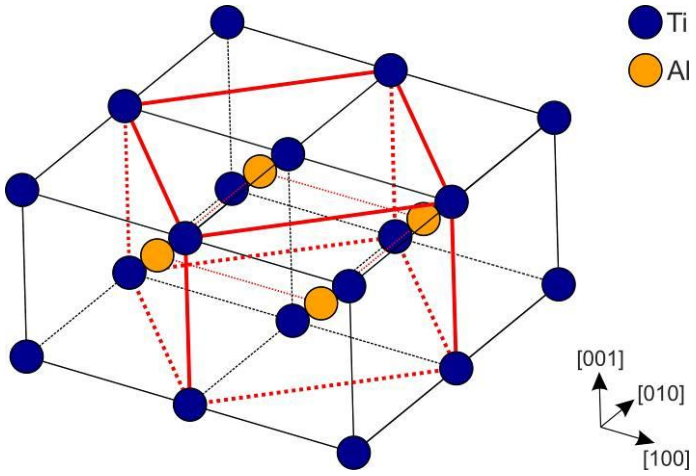

Fig. 7: Structural relationship between the stoichiometric β_o (B2 structure) and γ ($L1_0$ structure) phase in Ti-50Al (at.%). Using bold continuous and dotted lines, the unit cell of the γ phase is indicated within the structure of four β_o unit cells prior to deformation. For the adjustment of correct lattice parameters regarding γ, a bi-axial compression along [100] and [010] and an elongation along [001] is required [44].

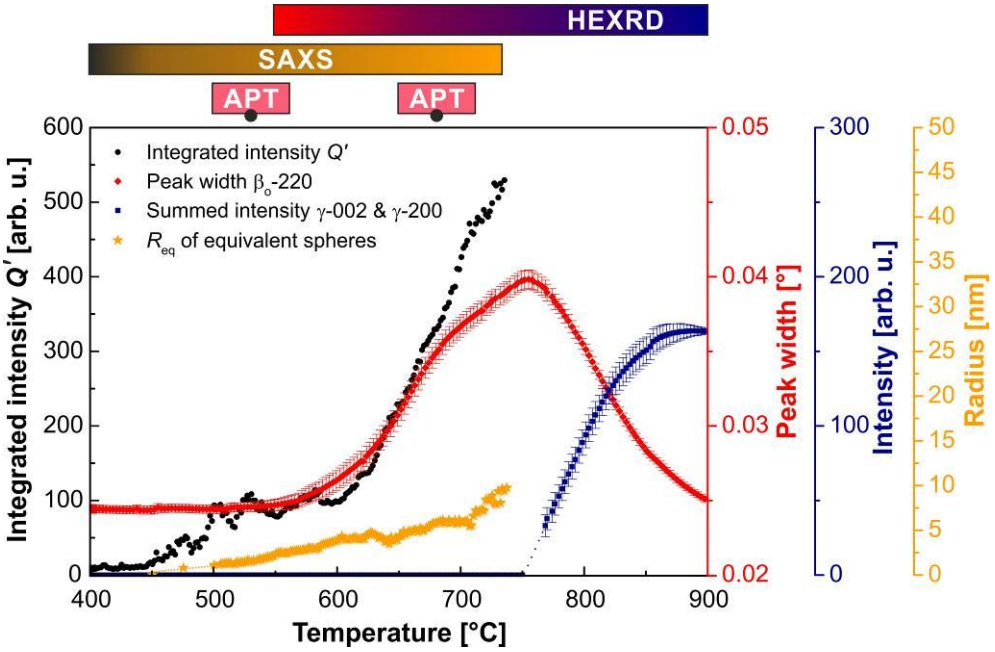

Fig. 8: Summary of selected key results obtained by means of *in situ* HEXRD and SAXS. The evolutions of the integrated intensity Q' and the equivalent radius R_{eq}, which were determined by means of SAXS, and those of the β_o-220 peak width and summed intensity of the γ-002 and γ-200 reflections, obtained by means of HEXRD, allow to trace the growth of the γ precipitates over a large temperature range. Furthermore, the strengths and limitations of the applied investigation techniques, including APT as direct imaging technique, are visualised in terms of covered temperature and size ranges.

Figure 1_colour_online only

Click here to download high resolution image

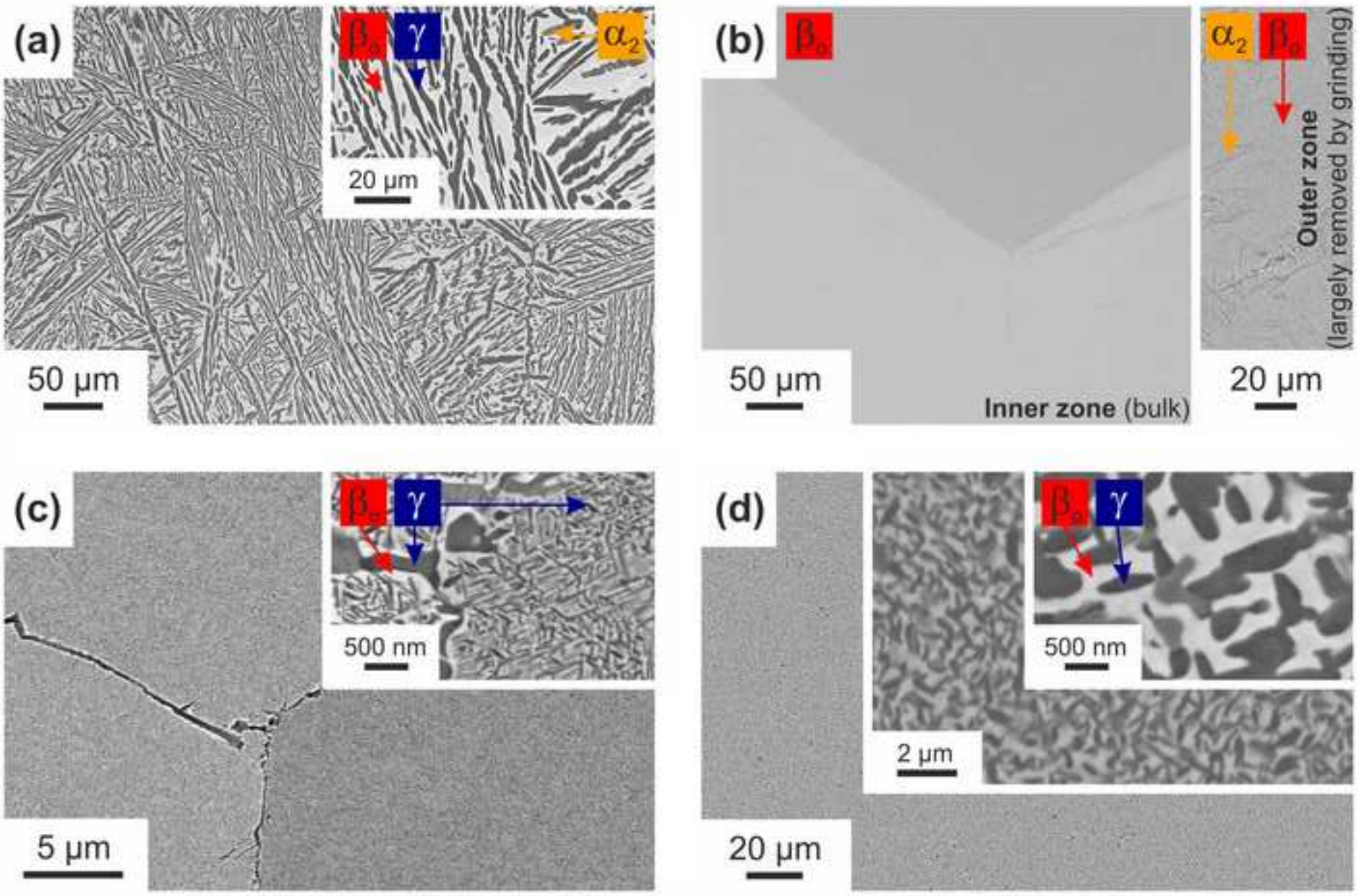

Figure 2_colour_online only

Click here to download high resolution image

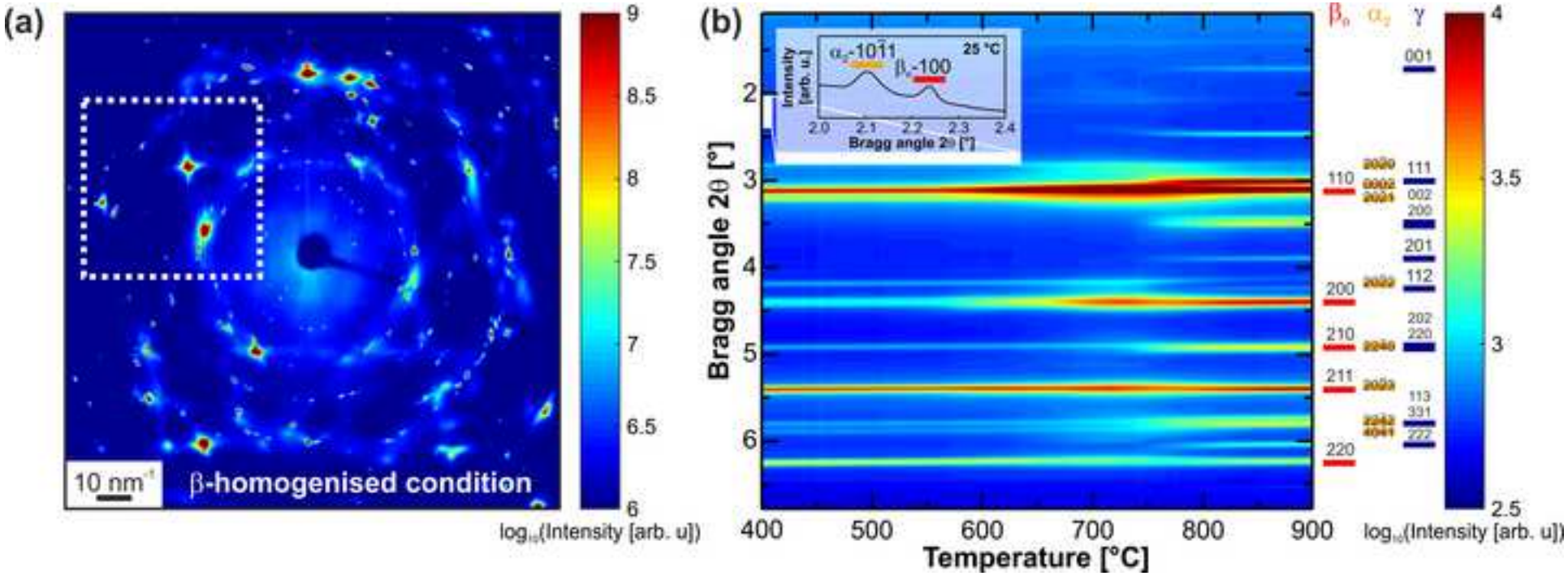

Figure 3_colour_online only

Click here to download high resolution image

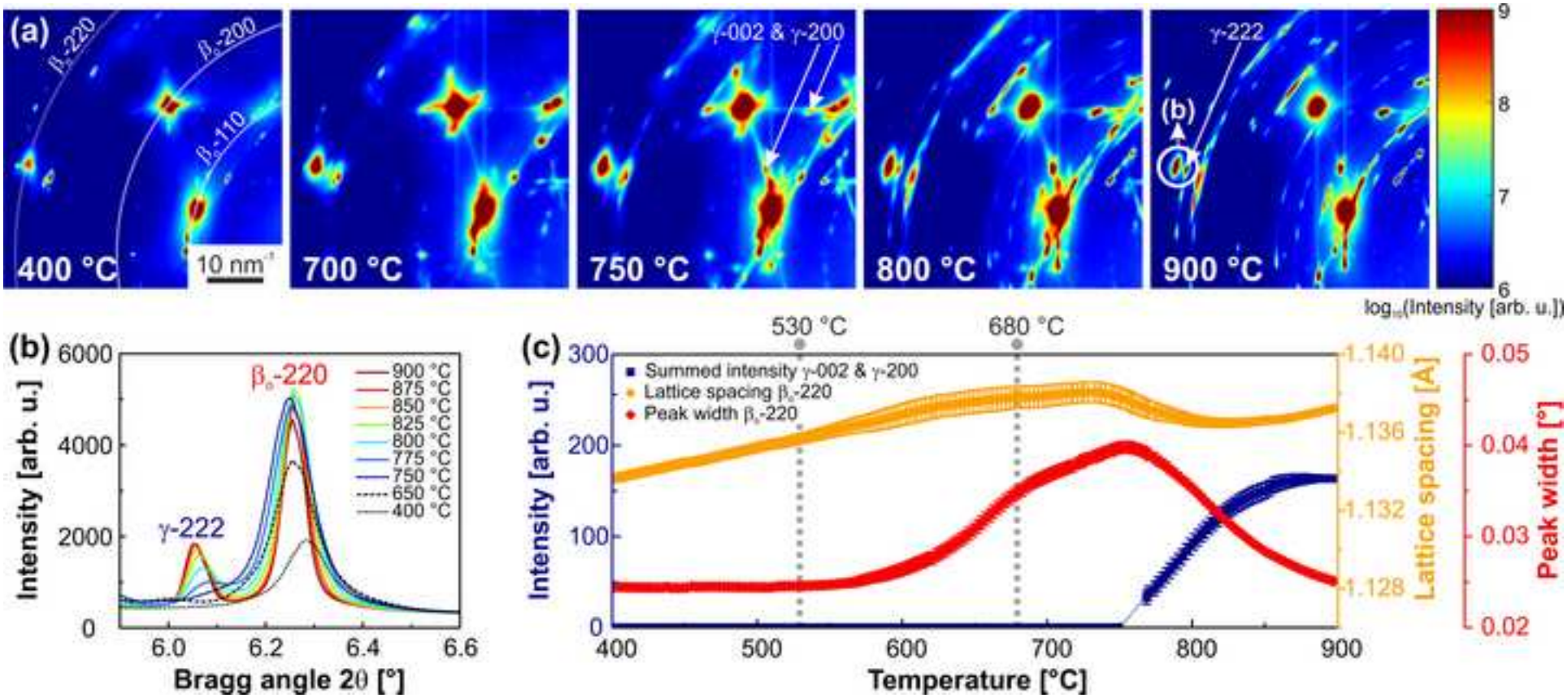

Figure 4_colour_online only

Click here to download high resolution image

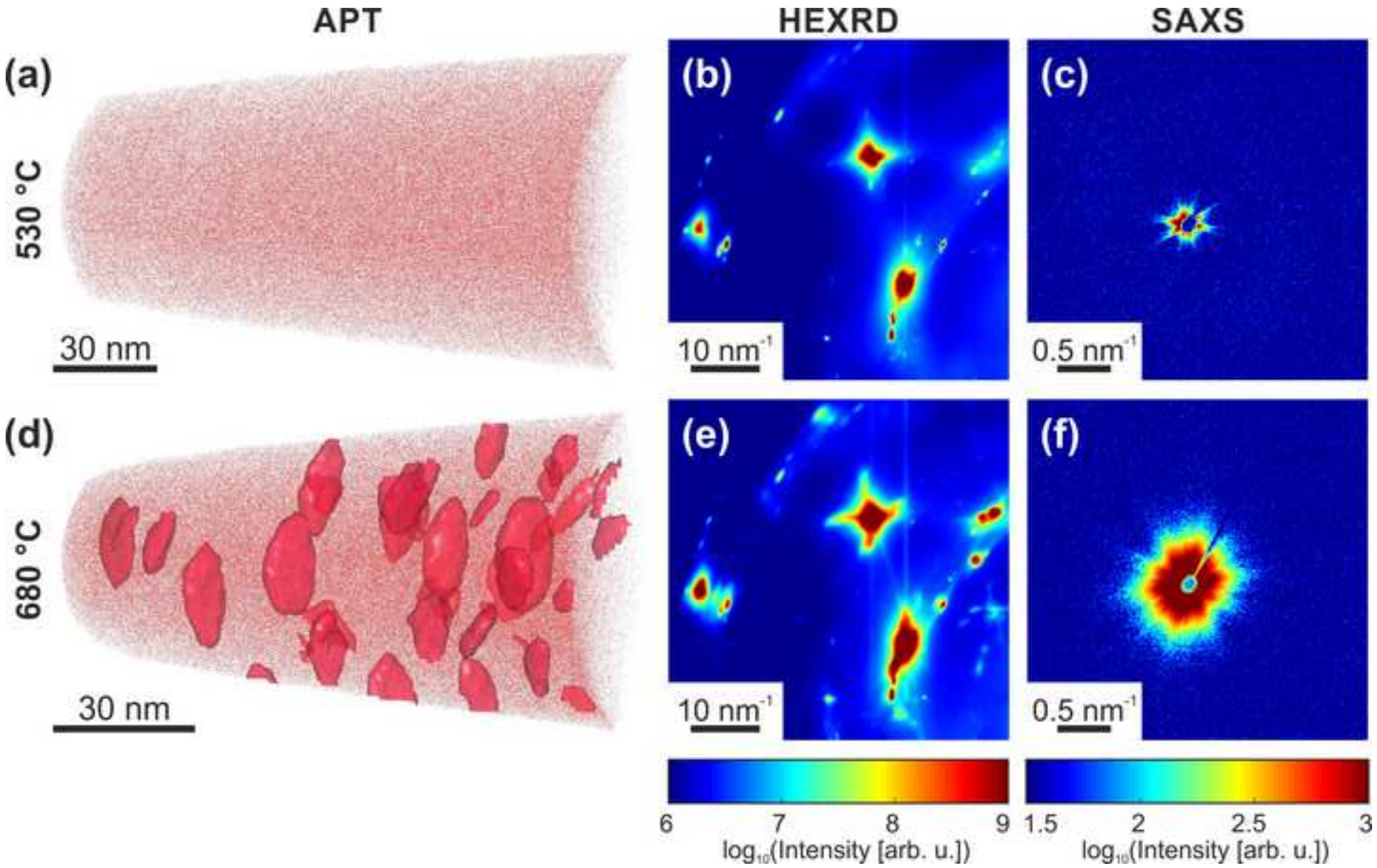

Figure 5_colour_online only

Click here to download high resolution image

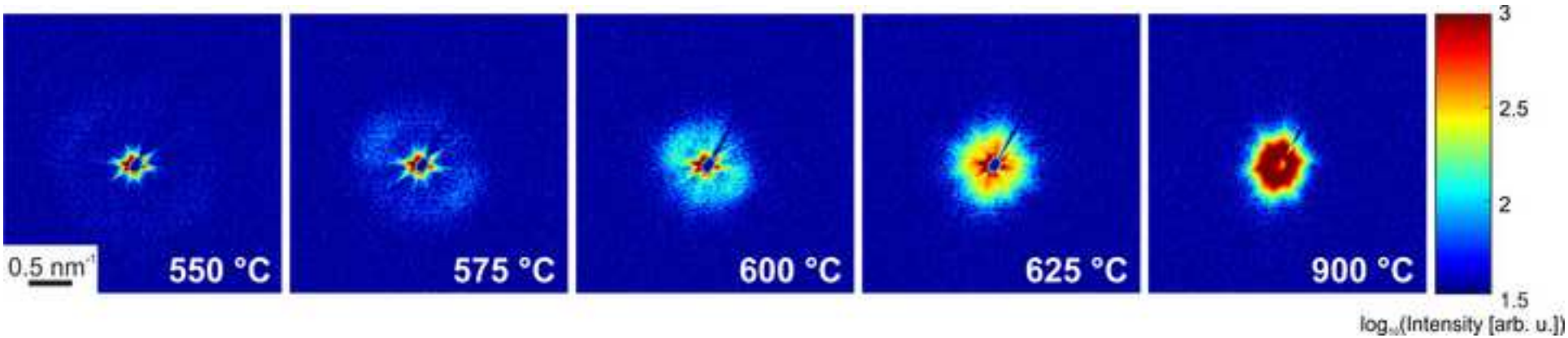

Figure 6_colour_online only

Click here to download high resolution image

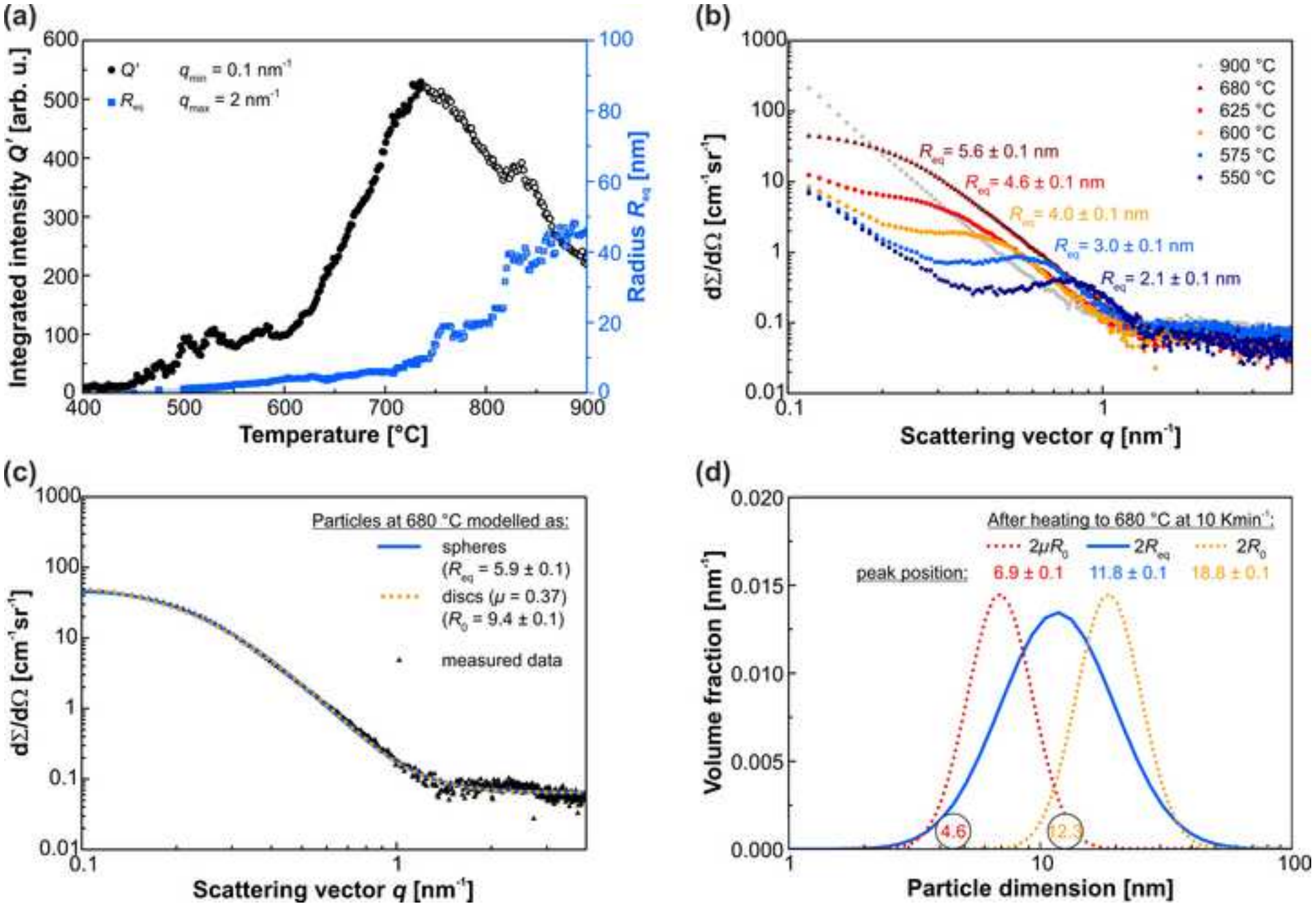

Figure 7_colour_online only

Click here to download high resolution image

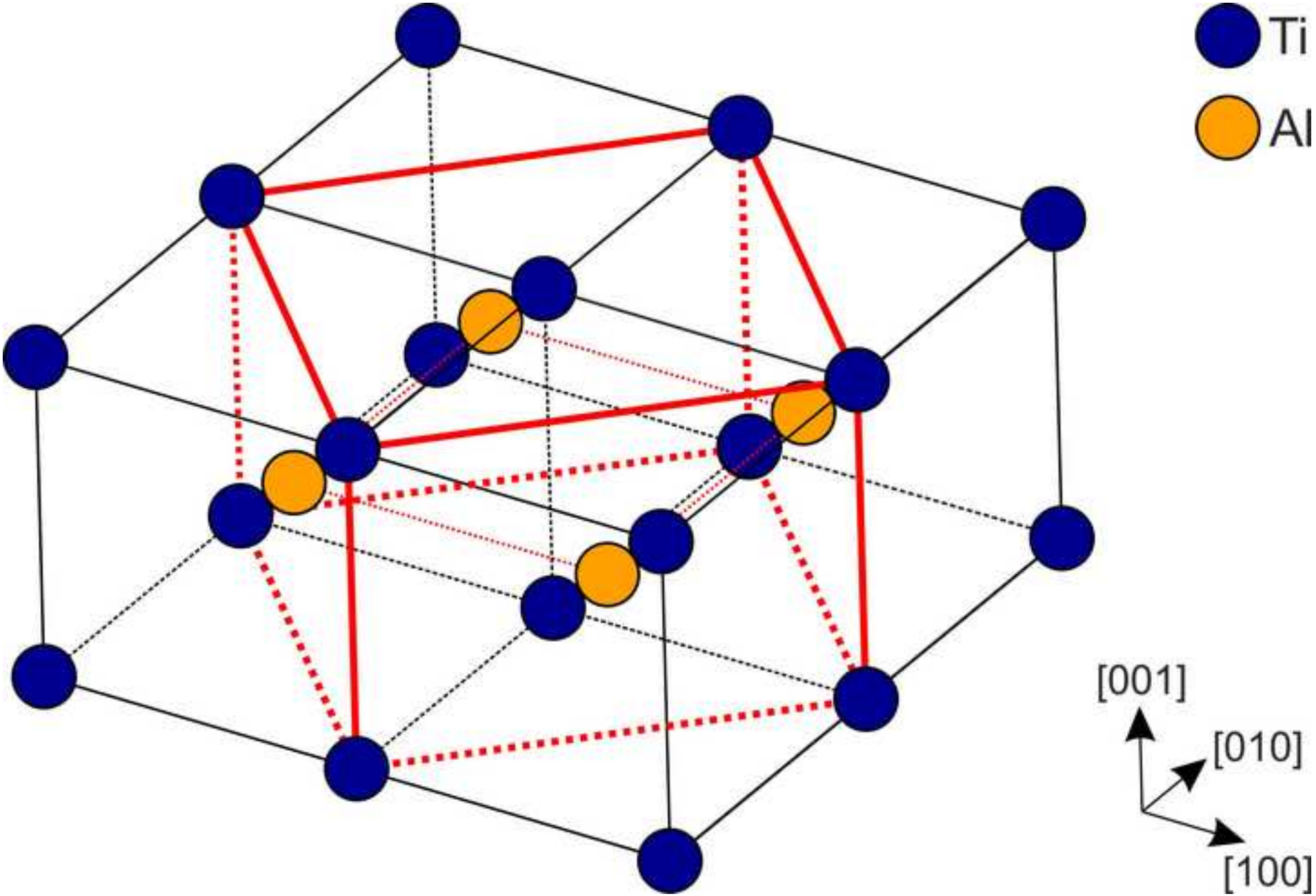

Figure 8_colour_online only
Click here to download high resolution image

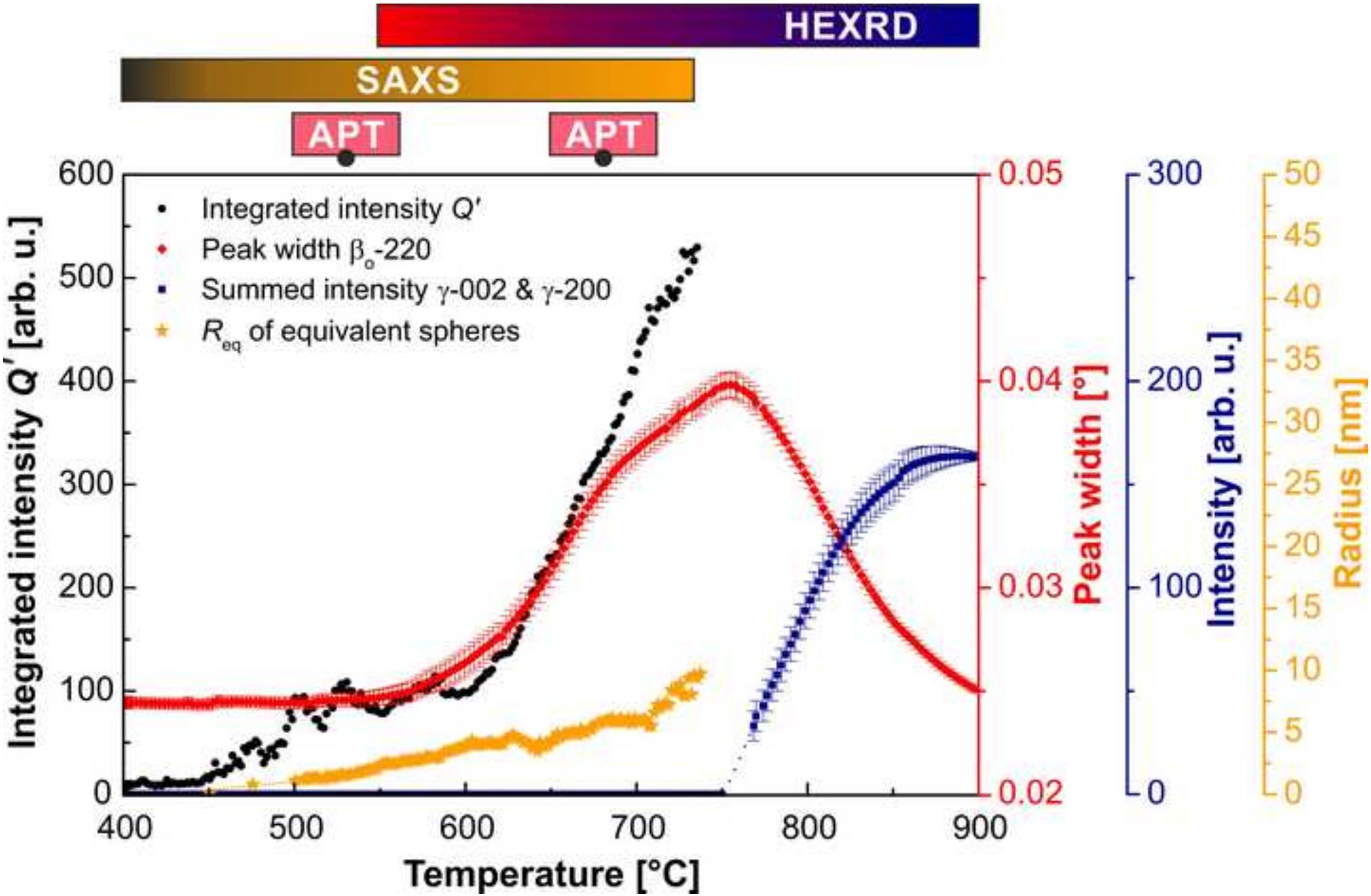

*Graphical Abstract